

**MICROSTRUCTURAL ANALYSIS OF Ni ALLOY CLADDING  
ONTO LOW ALLOY STEEL**

**QINGHUA ZHAO**

**B.S. Central-South University of Technology, P. R. China, 1985**

**M.S. Central-South University of Technology, P. R. China, 1988**

**A thesis submitted to the faculty of the  
Oregon Graduate Institute of Science & Technology  
in partial fulfillment of the requirements  
for the degree  
Master of Science  
in  
Materials Science and Engineering  
January 1993**

The thesis "Microstructural Analysis of Ni Alloy Cladding Onto Low Alloy Steel" by Qinghua Zhao has been examined and approved by the following Examination Committee:

---

Jack H. Devletian

Professor and Thesis Advisor

---

William E. Wood

Professor, Dept. Chairman

---

Lemmy L. Meekisho

Assistant Professor

## **ACKNOWLEDGEMENT**

The author gratefully acknowledges the National Center for Excellence in Metalworking Technology, Concurrent Technologies Corporation, and the U. S. Navy for providing partial financial support of this research.

This work would not have been possible without the encouragement, enthusiasm and support of my research advisor, Dr. Jack Devletian. Special thanks are also extended to Dr. W. E. Wood and Dr. L. Meekisho for their time and effort in evaluating the thesis.

I would also like to thank Youping Gao, Jack MaCarthy, Deva Ramaswamy, Vivek Dikshit, Jodi Buckintin and especially John Simmons, and all other students, staff and faculty in Materials Science & Engineering at Oregon Graduate Institute of Science & Technology, for their friendship and technical assistance.

## Table of Contents

Title Page	i
Approval Page	ii
Acknowledgements	iii
Table of Contents	iv
List of Tables	vii
List of Figures	viii
Abstract	xii
I. Introduction	1
II. Background	3
A. Electroslag Surfacing (ESS)	3
B. Ni Alloy 625	4
1. Solidification Behavior	4
2. Major Constituents in the Ni-Base Alloys	7
3. Solidification-Cracking in Nickel-Base Alloy	8
C. HAZ Microstructure of Carbon Steel	9
1. Upper Bainite	10
2. Lower Bainite	11
3. Martensite	11
4. Tempered Martensite	12
III. Experimental Procedures	13
A. Materials and Cladding Processes	13
B. Microstructure Examination	13
1. Optical Microscopy	13
2. Scanning Electron Microscopy	15

3. Transmission Electron Microscopy .....	16
4. Extraction Replica Preparation .....	16
C. Mechanical Testing .....	17
IV. Results and Discussion .....	18
A. Evaluation of Cladding Layers .....	18
1. Chemical Analysis .....	18
2. Microstructure Examination .....	19
(a) Optical Microscopy .....	19
(b) Image Analysis .....	21
(c) Scanning Electron Microscopy .....	21
(d) Transmitted Electron Microscopy .....	25
(e) Extraction Replica .....	31
(f) Elemental Segregation .....	35
3. Tensile Testing .....	36
4. Summary .....	39
B. ESS Cladding Interface Characterization .....	42
1. Microhardness .....	42
2. Composition Variations .....	43
3. Optical Microscopy .....	44
4. Analytical Electron Microscopy .....	46
(a) ESS Cladding Interface in the As-Welded Condition ..	46
(b) ESS Cladding Interface after PWHT .....	51
(c) Summary .....	53
C. Effect of Preheat Temperature on HAZ Microstructure .....	54
1. 93°C .....	55
2. 150°C .....	57
3. 204°C .....	63
4. Summary .....	63

<b>V. Conclusions</b> . . . . .	<b>66</b>
<b>Future Work Recommendations</b> . . . . .	<b>67</b>
<b>References</b> . . . . .	<b>68</b>
<b>Bibliographical Note</b> . . . . .	<b>74</b>

## List of Tables

Table 1:	Chemical Compositions of the Base Metal Steel and Ni Alloy Strip Electrodes . . . . .	14
Table 2:	Major Chemical Ingredients of the Fluxes . . . . .	15
Table 3:	Chemical Analysis of Single Layer Cladding . . . . .	18
Table 4:	Phase Compositions Determined by STEM/EDS . . . . .	35
Table 5:	Tensile Properties of the Single Layer Cladding . . . . .	37
Table 6:	Solidus Temperature ( $T_S$ ) and the Melting Range ( $\Delta T$ ) of the Cladding . . . . .	40
Table 7:	Effect of Preheat Temperature on the HAZ Microstructure . . . . .	65

## List of Figures

Figure 1:	Schematic Drawing of the ESS and SAS Processes . . . . .	3
Figure 2:	Optical Micrographs of the Cladding Layers in Conditions (a) ESS, As-Welded, (b) ESS, PWHT, (c) SAS, As-Welded, (d) SAS, PWHT. . . . .	20
Figure 3:	Image Analysis of the Interdendritic Precipitates with (a) Area Fraction and (b) Average Size. . . . .	22
Figure 4:	Backscattered Electron Images of the Cladding Microstructure in Conditions (a) ESS, As-Welded, (b) ESS, PWHT, (c) SAS, As-Welded, (d) SAS, PWHT. . . . .	23
Figure 5:	Higher Magnification of Figure 3(d). . . . .	24
Figure 6:	TEM Micrographs of ESS Cladding Showing Laves Phase in (a) Bright Field, (b) Centered Dark Field Taken with Reflection $[1\ 1\ \bar{2}\ \bar{2}]$ , and (c) the associated SAD Pattern at $[\bar{2}\ 4\ \bar{2}\ 3]$ Zone Axis. . . . .	26
Figure 7:	TEM Micrographs of ESS Cladding Showing Laves Phase in (a) Thin-Film Morphology and (b) the SAD Pattern at $[\bar{2}\ 4\ \bar{2}\ 3]$ Zone Axis. . . . .	27
Figure 8a:	TEM Micrograph of ESS Cladding Showing Laves Phase in Island Morphology . . . . .	28
Figure 8b:	TEM Micrograph of ESS Cladding Showing Small MC Carbides (Arrows) Attached to the Laves Phase. . . . .	28
Figure 9:	TEM Micrographs of ESS Cladding Showing (a) MC Carbides in Blocky Morphology and (b) the SAD Pattern at $[0\ 0\ 1]$ Zone Axis. . . . .	29

Figure 10:	TEM Micrographs of ESS Cladding Showing MC Carbides in (a) Dendritic Morphology and (b) the SAD Pattern at $[1\ 1\ 0]$ Zone Axis. . . . .	30
Figure 11:	Extraction Replica Obtained from the ESS Cladding Layer in As-Welded Condition. . . . .	32
Figure 12:	Extraction Replica Obtained from the ESS Cladding Layer in the As-Welded Condition Showing the MC Carbides in (a) Dendritic and (b) Blocky Morphologies. . . . .	33
Figure 13:	EDS Spectra of the (a) Laves phase, (b) MC Carbides. . . . .	34
Figure 14:	Elemental Segregation Profiles Across Dendrites of ESS Cladding in the As-Welded Condition. . . . .	36
Figure 15:	Fractographs of the Tensile Specimens in Conditions (a) ESS, As-Welded, (b) ESS, PWHT, (c) SAS, As-Welded and (d) SAS, PWHT. . . . .	38
Figure 16:	Microhardness Profiles Across the Interface of ESS Cladding in the As-Welded Condition. . . . .	42
Figure 17:	Chemical Composition Profiles Across the Interface of ESS Cladding in the As-Welded Condition. . . . .	43
Figure 18:	Optical Micrograph of the Base Metal. . . . .	44
Figure 19:	Optical Micrographs of the Cladding Interface Deposited by ESS in Conditions (a) As-Welded, (b) PWHT. . . . .	45
Figure 20:	TEM Micrographs of the ESS Cladding Interface in the As-Welded Condition, (a) BF and (b) the SAD Pattern from the Area A at $[0\ 1\ 3]_y$ zone axis, (c) SAD Pattern from the Area B at $[1\ 1\ 1]_x$ zone axis, (d) SAD pattern from the Area C at $[\bar{1}\ 3\ 3]_x$ zone axis. . . . .	47

Figure 21:	TEM Micrographs of the ESS Cladding Interface in the As-Welded Condition Showing the Retained Austenite Films in (a) BF, (b) CDF, Using Reflection $g = [1\ 1\ 0]_r$ , and (c) the SAD Pattern with superimposed zones of $[2\ 1\ \bar{1}]_r$ and $[3\ 1\ \bar{1}]_\alpha$ . . . . .	48
Figure 22:	TEM Micrographs of the ESS Cladding Interface in the As-Welded Condition Showing (a) the Fine Twins near the Fusion Line Labelled as T, and (b) the SAD Pattern from Area A at $[0\ 1\ 1]_r$ Zone Axis, (c) SAD Pattern from Area B at $[1\ 1\ 1]_\alpha$ Zone Axis. . . . .	49
Figure 23:	Chemical Composition Profiles Across the ESS Cladding Interface in the As-Welded Condition. . . . .	50
Figure 24:	TEM Micrograph of the ESS Cladding Interface After PWHT Showing Tempered Martensite with the Formation of Fine Carbides. . . . .	52
Figure 25:	$\gamma \rightarrow \alpha$ Phase Transformations . . . . .	54
Figure 26:	TEM Micrographs of Cementite Formed in the HAZ of the 93°C Preheated Specimens . . . . .	55
Figure 27:	TEM Micrograph Obtained from the HAZ of the 93°C Preheated Specimens Showing Lower Bainite with Fine Carbides inside the Laths. . . . .	56
Figure 28:	TEM Micrograph of Lath Martensite Formed in the HAZ of the 93°C Preheated Specimens. . . . .	56
Figure 29:	TEM Micrograph of Upper Bainitic Carbides Formed in the HAZ of the 150°C Preheated Specimens. . . . .	57
Figure 30:	TEM Micrographs of Auto-Tempered Martensite Formed in the 150°C Preheated Specimens in (a) BF and (b) CDF Images. . . . .	59
Figure 31:	TEM Micrographs of Twinned Martensite Formed in the 150°C Preheated Specimens in (a) BF, (b) CDF, Using Reflection $g = [0\ \bar{1}\ 1]_T$ , (c) SAD Pattern and (d) Index of (c). . . . .	60

Figure 32:	TEM Micrographs of the Twinned Martensite Formed in 150°C Preheated Specimens, (a) BF and (b) Carbides Precipitated on the Twins. . . . .	61
Figure 33:	TEM Micrographs of the Twinned Martensite Formed in the 150°C Preheated Specimens. . . . .	62
Figure 34:	TEM Micrographs of the Lath Martensite Formed in the 150°C Preheated Specimens. . . . .	63
Figure 35:	TEM Micrographs of the Auto-Tempered Martensite Formed in the 200°C Preheated Specimens with the Fine Carbides Lying in Three Directions. . . . .	64
Figure 36:	TEM Micrographs Showing the Mixed Microstructure of Lower Bainite (LB) and Upper Bainite (UB) in 200°C Preheated Specimens. . . . .	64

## ABSTRACT

### Microstructural Analysis of Ni Alloy Cladding onto Low Alloy Steel

Qinghua Zhao, M.S.

Oregon Graduate Institute of Science & Technology, 1992

Supervising Professor: Jack H. Devletian

Electroslag surfacing (ESS) with strip electrodes has been shown to provide lower dilution, lower penetration and higher deposition rate compared to submerged arc surfacing (SAS). The application of the ESS to clad Ni alloy 625 onto main propulsion shafting has created a need for microstructural analysis of the cladding layers, the interfacial regions, and the heat-affected zone (HAZ) of the low alloy steel. A comprehensive comparison of the cladding deposited by both ESS and SAS was also performed in this study.

The microstructure was examined using optical microscopy, scanning electron microscopy (SEM) and analytical electron microscopy (AEM). The cladding microstructure of the Ni-base alloy deposited by ESS and SAS processes consisted of matrix( $\gamma$ ) and interdendritic precipitates, (Nb, Mo)-rich MC carbides and Laves phase. During the solidification of the Ni-base alloy, Nb, Mo and Si segregated into interdendritic regions and promoted the formation of the (Nb, Mo)-rich MC carbides and Laves phase.

The cladding produced by the ESS process exhibited more favorable microstructure and had higher tensile ductility than the cladding from the SAS process. ESS cladding resulted in lower contents of Fe, C, Si and O, fewer oxide inclusions, lesser amount of Laves phase and higher ductility. The interdendritic precipitates in the ESS cladding were also small and isolated from each other. The lower ductility of the SAS cladding was found to be related to the many oxide inclusions and the formation of

the coarse, inter-connected, eutectic-like interdendritic (Nb, Mo)-rich MC carbides and Laves phase.

The interface between the steel base metal and the Ni alloy 625 cladding consisted of a thin region of martensite with about 0.5  $\mu\text{m}$  in thickness, in the as-welded condition of the ESS Cladding. After the stress-relieving at 604°C for two hours, the martensite was tempered with the formation of many fine carbides inside the laths. The HAZ microstructure was strongly affected by the preheat temperature for the ESS cladding. As the preheat temperature changed from 93°C to 204°C, the dominant microstructure in the HAZ varied progressively from (untempered martensite + lower bainite), to (upper bainite + auto-tempered martensite), and to auto-tempered martensite, respectively. Twinned martensite formed in the HAZ was due to the high substitutional solute concentrations of Ni and Cr.

In summary, the microstructural analysis showed that Ni alloy 625 could be successfully cladded over Ni-Mo steel without significant detrimental effects. Compared to SAS cladding, cladding layers deposited by ESS exhibited superior ductility, lower levels of oxides, Laves phase and MC carbides.

## I. INTRODUCTION

Electroslag surfacing (ESS) and submerged arc surfacing (SAS) using strip electrodes are known to be the most productive methods for cladding thick-section steels. Recent studies<sup>(1-6)</sup> have shown that ESS provides many advantages over SAS which include: (1) lower dilution, (2) lower penetration and (3) higher deposition rate. Until now, this highly efficient strip cladding process has not been widely used in the USA. As a result, a program sponsored by the U. S. Navy ManTech Office was initiated to clad Ni alloy 625 onto main propulsion shafting.

Nickel alloy 625 has excellent pitting and crevice corrosion resistance and has been widely used in chemical-processing equipment, ship and submarine parts, and nuclear reactors. Although having better weldability than INCONEL 718, Ni alloy 625 has also been found to be susceptible to solidification cracking during fusion welding due to the formation of low melting point eutectic-like constituents such as Nb-rich carbides and Laves phase.<sup>(7-22)</sup>

Nickel alloy 625 cladding deposited on a low alloy steel, offers the advantage of the high corrosion resistance of the nickel alloy and the low cost and good mechanical properties of the steel. The chemical compositions of Ni alloy 625 and the alloy steel are given in Table 1. Two possible problems are excessive iron dilution and irregular penetration patterns. Excessive dilution of iron maybe overcome by multilayer cladding, but this requires more material and energy. Excessive iron dilution and irregular penetration can result in a degradation of mechanical properties.<sup>(23-26)</sup> Previous studies of dissimilar metal joints have mainly focused on the stainless steel/carbon steel system.<sup>(27-32)</sup> Weldability and mechanical properties of Ni alloy 625 cladding and the interface characteristics of Ni alloy 625/steel joint deposited by electroslag surfacing with strip electrodes have not previously been studied in detail.

The objectives of this study were to: (1) evaluate and compare the microstructure and mechanical properties of the claddings deposited on a hardenable low alloy steel by ESS and SAS using Ni alloy 625 strip electrodes, (2) characterize the microstructure at the Ni alloy 625/steel interface, and (3) examine the effect of preheat temperature on the heat-affected zone microstructure of the base metal.

## II. BACKGROUND

### A. Principle of Electroslag Surfacing

Electroslag surfacing has been widely used in Europe since its introduction in 1971.<sup>(3)</sup> The mechanism of heat generation during the ESS process is different from that of SAS as shown in Figure 1. Instead of being derived from an electric arc as in the SAS process, heat is generated during ESS by ohmic resistance heating ( $I^2R$ ) of the molten slag as a result of current flowing through the strip and through the electroconductive slag. The electroslag surfacing process using strip electrodes has been shown to have substantially greater deposition rate with much less dilution compared to SAS.<sup>(1-6)</sup>

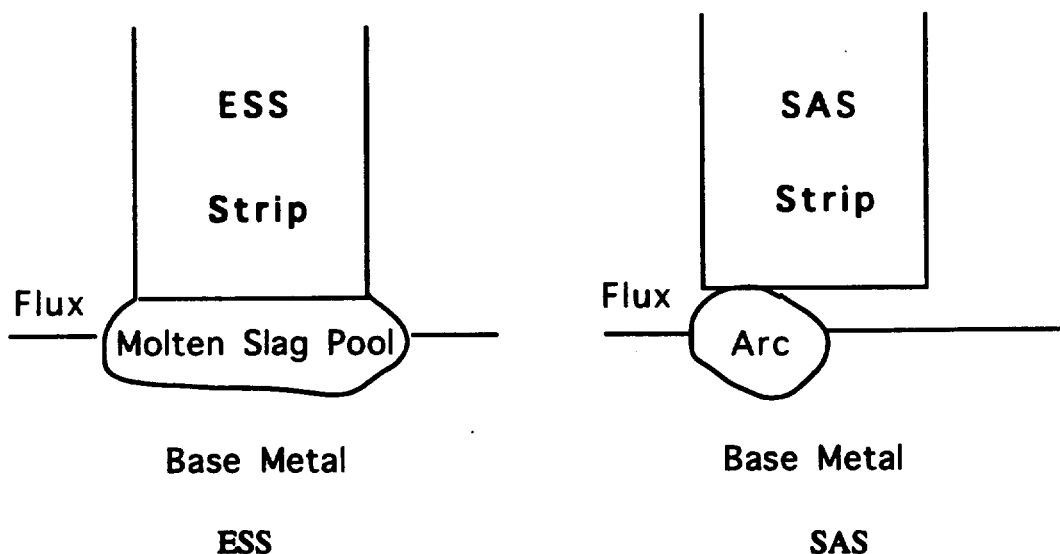


Figure 1. Schematic Drawing of the ESS and SAS Processes.

## B. Nickel Alloy 625

Nickel alloy 625 is based upon the ternary system Ni-Cr-Mo, with an addition of Nb that acts with Mo to stiffen the alloy matrix and thereby provides the high strength through solid-solution hardening. The alloy resists a wide range of severely corrosive environments and is especially resistant to pitting and crevice corrosion, and therefore has been widely used in chemical processing, aerospace and marine engineering, pollution control equipment, and nuclear reactors.<sup>(34)</sup>

### 1. Major Constituents in the Ni-Base Alloys

The matrix of the Ni-base alloys has a face-centered cubic (fcc) crystal structure. The space group is Fm3m and lattice parameter  $a = 0.357\text{nm}$ . The matrix contains solid solution strengtheners whose strengthening effects are proportional to the difference in the atom size between the nickel and solute atoms. Chromium, Mo and W are the most effective strengthening elements. In addition to the matrix, there are many constituents and precipitates which can form in nickel-base alloys depending on the chemical composition and the heat-treatment condition.<sup>(20,34,39-41)</sup> Three groups of phases are reviewed, which are (1) precipitates formed by heat-treatment, (2) carbides and (3) topologically-close-packed (TCP) phases. Precipitates formed during thermal treatment such as  $\gamma'$  and  $\gamma''$  are obtained to provide precipitation-hardening effect. Carbides can form during heat-treatment or solidification process. MC carbides are usually the solidification products, although precipitation and decomposition of MC carbides can also occur during heat-treatment. TCP phases appearing during solidification are detrimental to the weldability and the deformability of the Ni-base alloys.

#### (a) Precipitates Formed by Heat-Treatment

**Gamma prime ( $\gamma'$ ):**  $\gamma'$  is based on the ordered fcc  $\text{Ni}_3\text{Al}$  where the Ni atoms located at the face centers of the cell and the Al atoms are at the cube corners. The space

group is Pm3m and the lattice parameter varies from  $a = 0.3561$  nm to  $0.3568$  nm. The  $\gamma'$  precipitates can strengthen the alloys in two ways. First, coherency strains make it difficult for dislocations to penetrate the precipitates. Secondly, antiphase boundary energy is created when dislocations penetrate  $\gamma'$  because of the ordered structure.

**Gamma double prime ( $\gamma''$ ):** Although  $\gamma'$  is the predominant strengthening phase in most precipitation hardenable nickel base superalloys, some alloys have been developed in which the major contribution to precipitation strengthening is derived from the metastable and ordered  $\gamma''$ . This phase ( $\text{Ni}_3\text{Nb}$ ) has a tetragonal crystal structure, belongs to the space group 14/mmm and lattice parameters are  $a = 0.362$  nm and  $c = 0.741$  nm.

**Delta phase ( $\delta$ ):**  $\delta$  phase ( $\text{Ni}_3\text{Nb}$ ) has a orthorhombic structure with space group Pmmm and lattice parameters  $a = 0.503$  nm,  $b = 0.425$  nm, and  $c = 0.457$  nm. The morphology of  $\delta$  phase normally is a plate though globular  $\delta$  particles have also been observed. Controlled  $\delta$  phase appears to have a beneficial effect on stress rupture ductility, however, the formation of a large amount of coarse delta plates degrades the strength of gamma double prime hardened superalloys. This phase has been found to occur in Ni alloy 625 only when aged at temperatures above  $750^\circ\text{C}$  or during long time heat - treatment (e.g. over 1000 hours) at temperature of about  $600^\circ\text{C}$ .

## (b) Carbides

Most Ni-base superalloys contain carbides either in the grain boundaries or within the matrix. The most commonly observed carbides are MC,  $\text{M}_{23}\text{C}_6$  and  $\text{M}_6\text{C}$  type.

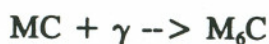
**MC carbides:** MC carbides have a blocky or chinese script morphology and cubic structure, the space group is Fm3m and lattice parameter is  $a = 0.43 - 0.47$  nm.<sup>(40)</sup> The prototype carbides that form are TaC, NbC, TiC and VC in order of decreasing stability. The formation of MC carbides are known to promote the solidification cracking in Ni-base alloys.<sup>(7-9)</sup>

**$\text{M}_{23}\text{C}_6$  carbides:**  $\text{M}_{23}\text{C}_6$  carbides have a complex cubic structure, the space group Fm3m, with lattice parameter ranging from  $a = 1.056 - 1.065$  nm.<sup>(40)</sup>  $\text{M}_{23}\text{C}_6$

carbides tend to form along grain boundaries and are abundant in high-chromium alloys. As with MC carbides, there can be considerable variation in the "M" content. The occurrence of  $M_{23}C_6$  carbides at grain boundaries tends to promote creep resistance by inhibiting grain boundary sliding.

**$M_6C$  carbides:**  $M_6C$  carbides also have a complex cubic crystal structure (diamond cubic in Ni alloy 625), Fd3m space group and lattice parameter ranging from  $a = 1.085 - 1.175$  nm.<sup>(41)</sup> This type of carbide also tends to precipitate at grain boundaries. The precipitate composition can vary widely, and formulas such as  $(Ni,Co)_2Mo_3C$  and  $(Ni,Co)_2W_4C$  have been suggested.

Carbides (MC,  $M_{23}C_6$  and  $M_6C$ ) may react with other phases to form other carbides and phases. The reactions generally occur relatively slowly, and in some cases may even continue over the life of the alloy. The following reactions have been shown to be important in nickel-base alloys.<sup>(41)</sup>



where  $\gamma$  represents the austenite,  $M'$  and  $M''$  represent metals in the matrix.

### (c) Topologically-Close-Packed Phases

The occurrence of brittle Topologically-Close-Packed (TCP) intermetallic phases, such as Laves phase and sigma phase, has a strong impact on the weldability and mechanical properties of the nickel-base superalloys.<sup>(7-8,14)</sup> All the TCP phases are generally deleterious and promote crack formation. Avoidance of TCP phases is incorporated in the new PHACOMP (for PHase COMPutation) scheme which is used in the development of new nickel-base superalloys.<sup>(42-43)</sup>

**Laves phase:** The compound formula of this phase takes the form  $M_2N$ , where  $M = Co, Cr, Fe, Ni$  and  $N = Nb, Mo$  or  $Ta$ . Laves phase has a hexagonal crystal structure and belongs to space group P63/mmc and lattice parameters  $a = 0.4744$  nm and  $c = 0.7725$  nm.<sup>(7)</sup>

**Sigma Phase ( $\sigma$ ):** Sigma phase ( $\sigma$ ) observed in nickel-base alloys has been identified as Mo-rich with a tetragonal structure and lattice parameters  $a = 0.908$  nm and  $c = 0.475$  nm.<sup>(14)</sup>

**P phase:** P phase has an orthorhombic structure and lattice parameters  $a = 0.907$  nm,  $b = 1.698$  nm, and  $c = 0.475$  nm.<sup>(14)</sup>

## 2. Solidification Behavior

The melting and solidification processes of Ni alloy 625 have been studied by Cieslak et al.<sup>(7-9)</sup> The effect of C, Si and Nb on the solidus ( $T_s$ ) and liquidus ( $T_L$ ) temperatures and the melting range  $\Delta T$  are given by the following equations:<sup>(7)</sup>

$$T_L = 1406.8 - 108.6 C - 27.8 Si - 11.1Nb \quad [1]$$

$$T_s = 1385.8 - 507.4 C - 48.6 Si - 20.6Nb \quad [2]$$

$$\Delta T = 20.9 + 405.5 C + 20.3 Si + 9.4Nb \quad [3]$$

where elements C, Si and Nb are in weight percentage (wt%) and the temperature is in degree centigrade ( $^{\circ}C$ ). From the above equations, it can be seen that the solidus and liquidus temperatures of Ni alloy 625 decrease and the melting range increases with increasing concentrations of C, Si and Nb.

The weld metal microstructure could also be affected by the concentration of C, Si, and Nb. Cieslak et al.<sup>(7-9)</sup> showed that the terminal solidification constituents in Nb-bearing alloys consisted of various combinations of  $\gamma/MC(NbC)$ ,  $\gamma$ /Laves phase and  $\gamma/M_6C$  eutectic-like constituents. The amount of each constituent varied with C, Si and Nb contents. Addition of C promoted the formation of MC carbides at the expense of the Laves phase. Silicon increased the formation of Laves phase and promoted the formation of  $M_6C$  carbide even at low carbon contents ( $< 0.01$  wt%). When both Si and C were present, both MC carbides and Laves phases were observed. It was proposed that the increased melting range and the formation of Nb-rich eutectic constituents were primarily responsible for the increased susceptibility of the Nb-bearing Ni-base superalloys to solidification cracking. Niobium-free alloys were observed to have a very low tendency toward solidification cracking, but even among those alloys,

C and Si were detrimental.<sup>(6)</sup>

### 3. Solidification-Cracking in Nickel-Base Alloys

There are two primary problems which occur in Ni-base alloys as a result of fusion welding processes, namely solidification-cracking and post-weld heat-treatment cracking.<sup>(44)</sup> Post-weld heat-treatment cracking is not generic to all superalloys but most significantly affects the  $\gamma'$  hardened superalloys. For example, Ni alloy 718 is designed to resist post-weld heat-treatment cracking which is chiefly attributed to the sluggish nature of the Nb-controlled  $\gamma'$  reaction. Solidification cracking is a serious problem for nickel base alloys during fusion welding. Although Ni alloy 625 has better weldability than Alloy 718,<sup>(44)</sup> solidification cracking in the weld metal and grain boundary liquation in HAZ have been observed.<sup>(7-9,18)</sup> Solidification-cracking in Ni-base alloys can be attributed to (1) deleterious elements (S, P, B) segregation at grain boundaries<sup>(35-38)</sup> and (2) low melting point constituents, MC carbides or Laves phase.<sup>(7-17)</sup>

#### (a) Effect of Minor Elements Upon Solidification Cracking

The presence of minor elements like S, P, B are deleterious to Ni-base alloy weldability. Solidification cracking in Ni-base alloys was observed along the interdendritic spaces of the weld metal where strong segregation of S and P were measured.<sup>(35-36)</sup> Electron microscopy also showed that the crack surfaces were covered with sulfides.<sup>(37-38)</sup>

Sulfur, P and B have very limited solubility in Ni and they all can form low temperature eutectic reactions with Ni or Ni compounds.<sup>(36)</sup> For example, the nickel-nickelsulfide eutectic reaction takes place at 650°C. In general, the effect of S, P and B was attributed to a high degree of segregation and subsequent reduction in the effective solidus and liquidus temperatures, which decreased the solid-liquid interfacial energy and permitted the wetting of the grain and subgrain boundaries and the subsequent formation of grain-boundary films.

### **(b) Low-Melting Point Eutectic Constituents**

Another important reason causing solidification cracking is the formation of low-melting eutectic-like constituents. It was reported that NbC and Laves phases promoted the solidification cracking in the weld HAZ of Ni alloys.<sup>(7-16,19)</sup> Solidification cracking in Ni alloy 718 has been found to be associated with intergranular liquation.<sup>(10-12,15,19)</sup> The low melting point eutectic-like Laves phase, niobium carbides and possibly borides were the sources of the intergranular liquid. The formation of the low melting eutectic-like carbides and Laves phase is dependent on several factors, such as bulk chemistry, chemical distribution, and microstructure prior to welding. Thompson<sup>(15)</sup> reported that when the carbon content increased from 0.02 to 0.06 wt%, the volume fraction of NbC carbide increased by 70%, but the volume fraction of Laves phase did not increase in a systematic manner with the carbon content. The increased volume fraction of carbides increased the solidification range and therefore increased the susceptibility to solidification cracking. Owczarski<sup>(16)</sup> examined the HAZ solidification cracking in Ni-base superalloy Udimet 700 and Waspaloy. Heat affected zone solidification cracking in both alloys was attributed to the grain-boundary liquation initiated in the vicinity of MC-type carbides and Laves phase.

Nickel alloy 625 is also susceptible to solidification cracking.<sup>(7-9,45)</sup> Solidification cracks in arc welds between Ni alloy 625 and 304L stainless steel were observed to be related to the presence of the low melting eutectic-like structures, and also the crack surfaces were found to be enriched with S, Nb, P and C. The weldability of Ni alloy 625 welded with gas tungsten arc (GTA) welding was studied by Cieslak,<sup>(8)</sup> who found that solidification cracking was associated with interdendritic low-melting constituents, such as Nb-rich MC carbides and Laves phase.

### **C. Heat-Affected-Zone Microstructure of Carbon Steel**

For dissimilar metal joints, the HAZ microstructure of the base metal steel is very difficult to predict, especially at the interfacial region between the weld metal and the

base metal due to the mixed composition. For Ni alloy 625 cladding over carbon steel, the phase transformations at the interface region were studied by Raghavan et al.<sup>(24)</sup> Two interesting features were observed; (1) a thin layer of untempered lath martensite located between fcc austenite and bcc ferrite, (2)  $M_{23}C_6$  carbides were detected at the boundary between the untempered martensite and the bcc ferrite.

Phase transformations within the HAZ of carbon steel can be very complex and difficult to predict. During a typical cladding or welding procedure, the HAZ will go through a complete thermal cycle, therefore, the  $\alpha \rightarrow \gamma$  transformation will occur in the heating cycle, and  $\gamma \rightarrow \alpha$  will occur during the cooling cycle.<sup>(46)</sup> Carbon atoms play a very important role during these phase transformations. Due to the lower solubility of carbon in  $\alpha$  than in  $\gamma$ ,  $\gamma \rightarrow \alpha$  transformation would normally lead to the rejection of carbon atoms to the  $\gamma$  phase boundaries. The products of the  $\gamma \rightarrow \alpha$  transformation are strongly affected by the cooling rate. Phases which could be formed are proeutectoid ferrite, pearlite, bainite and martensite, which form in an increasing order of the cooling rate.<sup>(47)</sup> The crystal structures and morphologies of upper bainite, lower bainite, martensite and tempered martensite will be briefly reviewed below.

### 1. Upper Bainite

Upper bainite consists of needle or lath ferrite with cementite precipitates between the laths. The solubility of carbon in upper bainite is lower than that in austenite, consequently, as the bainitic laths grow, the carbon atoms diffuse to the lath boundaries where the remaining austenite exists, and form cementite ( $Fe_3C$ ). Ferrite laths grow into austenite in a similar way to Widmanstätten side-plates.<sup>(50)</sup> The ferrite nucleates on a grain boundary with a Kurdjumov-Sachs orientation relationship with one of the austenite grains. The austenite and cementite are related to Pitsch relationship:<sup>(50)</sup>

$$(0\ 0\ 1)_c // (\bar{2}\ 2\ 5)_\gamma$$

$$[1\ 0\ 0]_c // [\bar{5}\ 5\ 4]_\gamma$$

$$[0\ 1\ 0]_c // [\bar{1}\ 1\ 0]_\gamma$$

## 2. Lower Bainite

Lower bainite is formed in the temperature range between upper bainite and martensite.<sup>(48)</sup> The growth of lower bainite is controlled by the rate of carbon diffusion away from the  $\gamma/\alpha$  interface, or the rate at which carbides can precipitate at the interface. In this case cementite forms with the Bagaryatski orientation relationship:<sup>(47)</sup>

$$(0\ 0\ 1)_C // (2\ 1\ 1)_\alpha$$

$$[1\ 0\ 0]_C // [1\ 0\ 1]_\alpha$$

$$[0\ 1\ 0]_C // [1\ 1\ 1]_\alpha$$

Unlike carbides in tempered martensite, cementite in lower bainite exhibits only one direction such that they form parallel arrays at about  $60^\circ$  relative to the main direction of the bainite laths.

## 3. Martensite

Martensite is a product of diffusionless phase transformations from austenite to ferrite.<sup>(48-49)</sup> The morphology of martensite can be lath, plate or mixed structure depending on the carbon content in the steel.<sup>(47,50)</sup> Lath martensite is the most commonly occurring martensite structure in low- and medium-carbon steels, the substructure of which consists of a high density of dislocations. The orientation relationship between the austenite ( $\gamma$ ) and the ferritic martensite ( $\alpha'$ ) can be described by Kurdjumov-Sachs relationship:<sup>(47)</sup>

$$\{1\ 1\ 1\}_\gamma // \{1\ 1\ 0\}_{\alpha'}$$

$$\langle 0\ 1\ 1 \rangle_\gamma // \langle 1\ 1\ 1 \rangle_{\alpha'}$$

and the habit plane varies from  $\{1\ 1\ 1\}_\gamma$  at low carbon contents, to  $\{2\ 2\ 5\}_\gamma$  at medium carbon contents. For high carbon steel, martensite usually forms in a plate morphology with a twinned substructure. The orientation relationship changes to Nishiyama:<sup>(47)</sup>

$$\{1\ 1\ 1\}_\gamma // \{1\ 1\ 0\}_{\alpha'}$$

$$\langle 1\ 1\ 2 \rangle_\gamma // \langle 0\ 1\ 1 \rangle_{\alpha'}$$

and the habit plane is  $\{259\}_\gamma$ . Martensite has a body-centered tetragonal (bct) crystal

structure, which is a distorted form of bcc iron. The tetragonality measured by the ratio between the axes,  $c/a$ , increases with the carbon content:  $c/a = 1 + 0.045 C$  (in wt%).<sup>(47)</sup>

#### 4. Tempered Martensite

Due to high cooling rates necessary for martensite formation in the alloys, the martensite is supersaturated with carbon atoms at the interstitial lattice positions in the parent austenite.<sup>(49)</sup> Upon aging or tempering, therefore, there is a strong driving force for carbide precipitation. The tempering of martensite includes diffusion of carbon, precipitation of carbides, decomposition of retained martensite and recrystallization. Therefore, a series of phase transformations can be expected during tempering. For the cladding process, if the martensite formation temperature  $M_s$  is above the room temperature, the HAZ martensite will go through an elevated temperature range in which tempering can occur. This process is called auto-tempering. The orientation relationship between the cementite and the ferrite laths obeys Bagaryatski relationship.<sup>(47)</sup> However, the carbides formed in the tempered martensite usually lie in several directions of variants instead of only one in the lower bainite.

### **III. EXPERIMENTAL PROCEDURES**

#### **A. Materials and Cladding Processes**

In the current study, a hardenable carbon steel (MIL-S-23284, Class 1 steel) was used as the base metal, and Ni alloy 625 as the strip electrodes. The nominal compositions of the materials are listed in Table 1. The base metal plate thickness was about 50 mm. The strip electrode size was 30mm wide and 0.5mm thick.

Two cladding methods were employed: Electroslag Surfacing (ESS) and Submerged Arc Surfacing (SAS). For comparison, the two cladding processes were performed under the same welding parameters at 650A, 27V and 152mm/min (6ipm), and also the base metal plates were preheated to 93°C (200°F) prior to the cladding. In this study, only a single cladding layer was deposited. The cladding was subsequently stress-relieved at 604°C for two hours. Both the as-welded and the stress-relieved conditions of the ESS and SAS cladding were examined. The major chemical ingredients of the fluxes used for ESS and SAS are given in Table 2. For the ESS process, three preheat temperatures [93°C (200°F), 150°C (300°F) and 204°C (400°F)] were used to study their effect on the HAZ microstructure of the base metal.

#### **B. Microstructure Examination**

##### **1. Optical Microscopy**

The metallographic specimens were taken from the cross section of the cladding bulk sample, which included both the cladding layer and the heat-affected zone (HAZ) of the base metal steel. The specimens were ground using water and SiC abrasive papers with grit sizes of 240, 320, 400, 600 and 800. Intermediate polishing was done with 6 and 1 micron diamond pastes. Final polishing was performed using a LECO final

<b>Table 1. Chemical Compositions of the Base Metal Steel and Ni Alloy 625 Strip Electrodes</b>		
<b>Elements, wt%</b>	<b>Ni alloy 625</b>	<b>Carbon steel</b>
C	0.03	0.25
Fe	4.25	bal.
Ni	61.02	3.252
Cr	21.52	0.427
Mo	9.02	0.442
Nb	<3.45	0.003
Mn	0.08	0.335
Si	0.09	0.221
Cu	0.33	0.093
Ti	0.20	0.001
Ta	<0.01	-
Al	0.32	0.005
S	<0.001	0.02
P	0.009	<0.001
Ta	<0.01	-
Co	-	0.009
V	-	0.059
W	-	0.018
other	0.5	-

automatic polishing unit and 0.05 micron cerium-oxide polishing solution.

As a result of the widely dissimilar compositions between the cladding layer and the base metal, the microstructure of the steel was revealed by using 2% nital solution which did not react with the Ni alloy 625. The Ni alloy 625 cladding layers were examined under unetched condition for both optical microscopy and the scanning electron microscopy.

Microstructural features were quantitatively analyzed using a image analysis unit connected to the optical microscope. At least 20 fields, randomly chosen, were used for each analysis. The average size and the area fraction of the second phases formed in the cladding layers were determined for each cladding specimen.

Ingredient	ESS (59s)	SAS
Al <sub>2</sub> O <sub>3</sub>	8	29
CaF <sub>2</sub>	80	16
CaO	0	24
SiO <sub>2</sub>	5	25
BaF <sub>2</sub>	6	0
Cr	0	3
K <sub>2</sub> O + Na <sub>2</sub> O	1	3

## **2. Scanning Electron Microscopy**

After examination using optical microscopy, the specimens were Au-Pd coated. The solidification structure of the cladding layers were examined using scanning electron microscopy (SEM) at a working voltage of 15 kv. SEM images were taken with backscattered electrons in order to show the atomic contrast between the matrix and precipitates.

Chemical analysis across the dendrites was performed with an SEM which was equipped with an energy dispersive spectrometer (EDS). The compositions were calculated based upon a semi-quantitative (SSQ) program.

### **3. Transmission Electron Microscopy**

Microstructure examination was also performed using a transmission electron microscope (TEM) at an operation voltage of 200 kv. Thin-foils of the Ni alloy 625 cladding layers were sliced and ground into about 100 microns in thickness using SiC abrasive papers with grit sizes of 400, 600 and 800. The samples were further polished to about 60 microns in thickness with 6 and 1 micron diamond pastes. Electropolishing was used as the final thinning process with a solution containing 10% perchloride and 90% methanol at -60°C.

For the samples from the interface area which included the Ni alloy 625 cladding layer and the carbon steel, the thin area was always obtained preferentially at one side of the interface when using electropolishing. Therefore, the ion-milling technique was used. The 3mm diameter discs containing the Ni alloy 625 cladding layer and the MIL-S-23284, Class 1, steel were ground to perforation, reinforced by laminating molybdenum washers to the discs and ion-milled until the interface was electron-transparent.

Chemical compositions of the interface region from the Ni-base cladding layer to the HAZ of the steel were generated by collecting x-ray spectra at regular intervals with the TEM in the scanning transmission mode. The spectra were then processed by a standardless metallurgical thin-film (SMTF) approximation program to produce the compositions at each point of analysis.

### **4. Extraction Replica Preparation**

Second phase particles formed in the cladding layers were removed from the matrix using carbon extraction replication. Metallographically polished specimens were

electrolytically etched using a 10% oxalic acid solution which etched the matrix and left the second phases in relief. A thin layer of carbon (estimated to be 30-60 nm in thickness) was evaporated onto the samples. The surface of each sample was scored into small squares (about 1 or 2 [mm]<sup>2</sup>) and subsequently etched electrolytically with a 10% HCl/methanol solution to dissolve the matrix and loosen-up the carbon film. When the carbon films started to separate from the surface, the samples were immersed in water and the carbon replica floated on the surface. The carbon extractions were then captured on 3mm diameter copper TEM grids.

The carbon extraction replica was examined using a TEM. Chemical composition data of the second phases was generated from the energy dispersive X-ray detector. Phase compositions were calculated using the program SMTF.

### **C. Mechanical Testing**

The Knoop microhardness was measured using a microhardness tester, with a 300g load and loading time 15 seconds. The specimens were polished using the metallographic specimen preparation procedures. Each specimen was tested three times at each distance from the joint line and the average data of the hardness was analyzed.

Flat tensile test samples were cut from the cladding layers of the ESS and SAS clads. The gage length and the thickness of the tensile specimens were 50mm (2") and 3.2mm (0.125"), respectively. Tensile tests were performed at room temperature. The ultimate tensile strength (UTS), yield strength (YS), elongation and reduction of area were measured.

## IV. RESULTS AND DISCUSSION

### A. Evaluation of Cladding Layers

#### 1. Chemical Analysis

Chemical analysis of the cladding layers was carried out using a spectroscopic analyzer. Table 3 shows the concentrations of Fe, C, Si, O and Nb. The SAS process resulted in higher concentrations of Fe, C, Si and O in the cladding layers. Iron and carbon in the cladding layers came primarily from the steel base metal. During the cladding process, the surface of the base metal was molten and mixed with the strip electrodes, therefore, Fe, C and other elements in the base metal steel were brought into the cladding layer. The higher the dilution level, the higher the concentration of Fe and C in the cladding. It has been reported that the ESS process provides lower dilution than similar cladding deposited by SAS.<sup>(1)</sup>

Element	ESS	SAS
Fe (wt%)	7.7	12.5
C (wt%)	0.04	0.05
O (ppm)	280	700
Si (wt%)	0.37	0.69
Nb (wt%)	3.0	3.0

Silicon and oxygen were introduced into the cladding layers as a result of molten metal-slag reactions during the cladding process. As shown in Table 2, the flux used for SAS contained 29%  $Al_2O_3$  and 25%  $SiO_2$ , while the flux used for ESS was

predominantly  $\text{CaF}_2$  (80%). The Si and O contents in the cladding was found to be strongly related to the basicity index (BI) of the fluxes.<sup>(26)</sup> The higher the basicity, the lower the concentration of Si and O in the cladding. The flux basicity index can be calculated using the following equation:<sup>(51)</sup>

$$\text{BI} = [\text{CaO} + \text{Na}_2\text{O} + \text{K}_2\text{O} + \text{CaF}_2] / [\text{SiO}_2 + 0.5 (\text{Al}_2\text{O}_3)]$$

The BI of the two fluxes used for ESS and SAS were calculated as 9 and 1.1, respectively. This explains why the SAS process resulted in higher concentrations of Si and O in the cladding layer.

## **2. Microstructure Examination**

### **(a) Optical Microscopy**

The optical micrograph in Figure 2 shows the typical microstructure of Ni alloy 625 cladding deposited on the low alloy steel. Generally, the cladding microstructure consisted of gamma ( $\gamma$ ) matrix and interdendritic constituents. Figure 2(a) and (b) show the microstructure of the ESS cladding in the as-welded and PWHT conditions, respectively. The optical micrographs show that the PWHT (604°C for 2 hours) did not change the as-welded cladding microstructure significantly. The SAS as-welded cladding microstructure is shown in Figure 2(c) and after PWHT in Figure 2(d). More large spheroidal inclusions were observed in the SAS cladding than in the ESS cladding as can be seen when comparing Figure 2(a) and (b) to Figure 2(c) and (d).

The optical micrographs show that the primary differences between the two cladding processes was that many oxide inclusions were produced by the SAS process. Those inclusions contain very high amount of Si or Al as determined from the energy dispersive X-ray analysis.



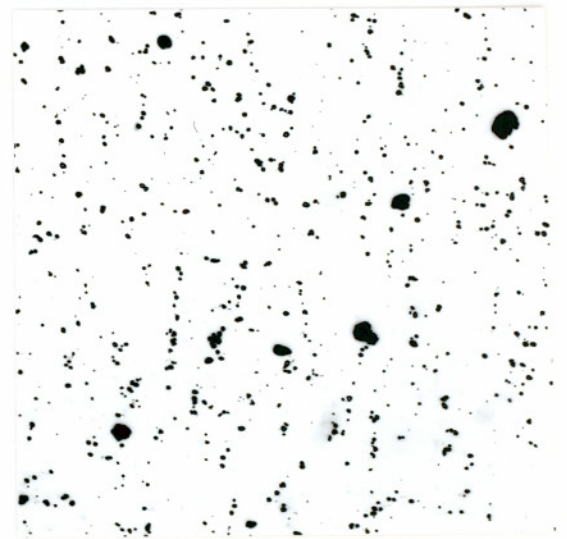
(a) 50  $\mu\text{m}$



(b) 50  $\mu\text{m}$



(c) 50  $\mu\text{m}$



(d) 50  $\mu\text{m}$

Figure 2. Optical Micrographs of the Cladding Layers in Conditions (a) ESS, As-Welded, (b) ESS, PWHT, (c) SAS, As-Welded, (d) SAS, PWHT.

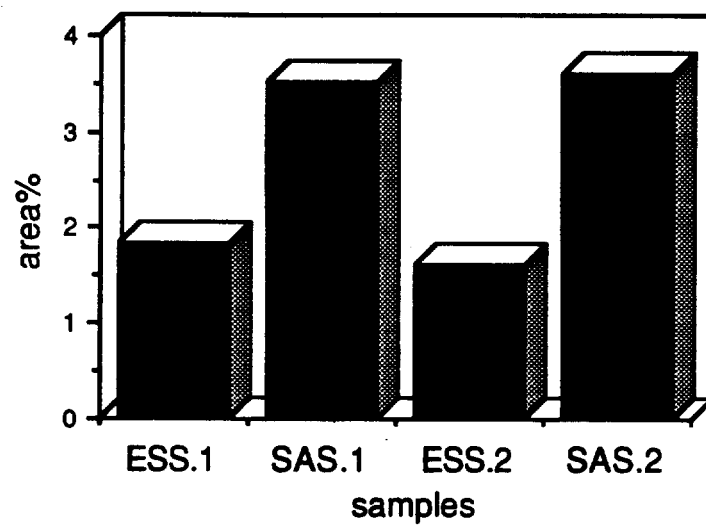
### **(b) Image Analysis**

The metallographic specimens of the ESS and SAS cladding were examined with an image analysis system. The area fraction and the average size of the interdendritic precipitates shown in the optical micrograph of Figure 2 were measured and the results plotted in Figure 3. Figure 3(a) shows the area fraction of the total precipitates. For the ESS specimens in either as-welded or PWHT conditions, the precipitate area fraction was about 1.8%, while the precipitate area fraction in the SAS cladding specimens was about 3.6% which is the double amount in ESS specimens. The average precipitate size is shown in Figure 3(b). The average size of the interdendritic precipitates in the ESS specimens was about  $4 \text{ } [\mu\text{m}]^2$ , and the average size in SAS specimens was  $5.8 \text{ } [\mu\text{m}]^2$ . The interdendritic precipitates in the cladding deposited by ESS had lesser area fraction and smaller average size than those in the SAS cladding.

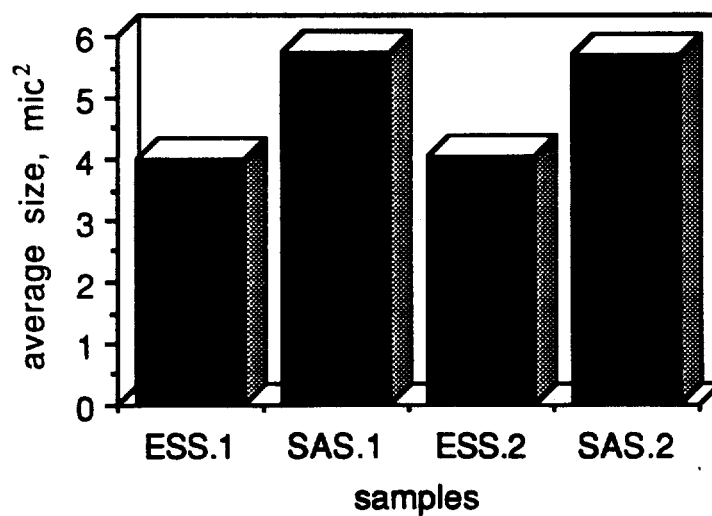
### **(c) Scanning Electron Microscopy**

Figure 4 shows the backscattered electron images of the ESS and SAS cladding microstructures. The contrast of the interdendritic precipitates was brighter than the matrix, which means their average atomic number was higher than the surrounding matrix.

The size and morphology of the interdendritic precipitates were different between the ESS and SAS cladding layers. The interdendritic precipitates in the ESS cladding, Figure 4(a) and (b), were small and isolated from each other. These precipitates generally had a blocky morphology. Figure 4(c) and (d) show the microstructure of the SAS cladding. The precipitates were coarse, inter-connected, and most of them had a eutectic-like structure. Figure 5 is a higher magnification photo taken from the same area shown in Figure 4(d). It clearly shows the eutectic-like interdendritic precipitates in the SAS cladding. The difference of the interdendritic precipitates produced by the two cladding processes will be explained in the summary part.



(a)



(b)

Figure 3. Image Analysis of the Interdendritic Precipitates with  
(a) Area Fraction and (b) Average Size.

Note: 1 -- As-Welded, 2 -- PWHT.

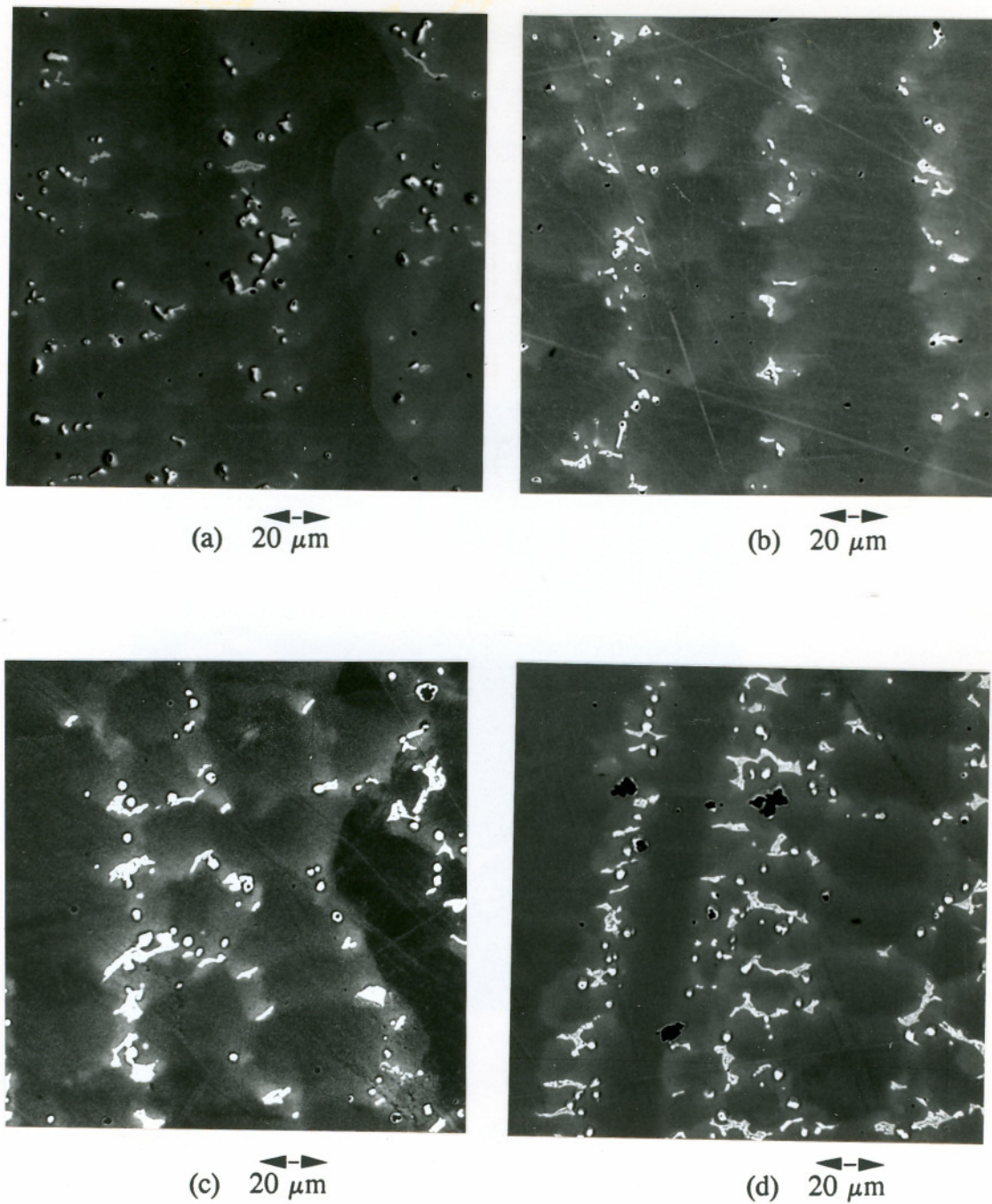
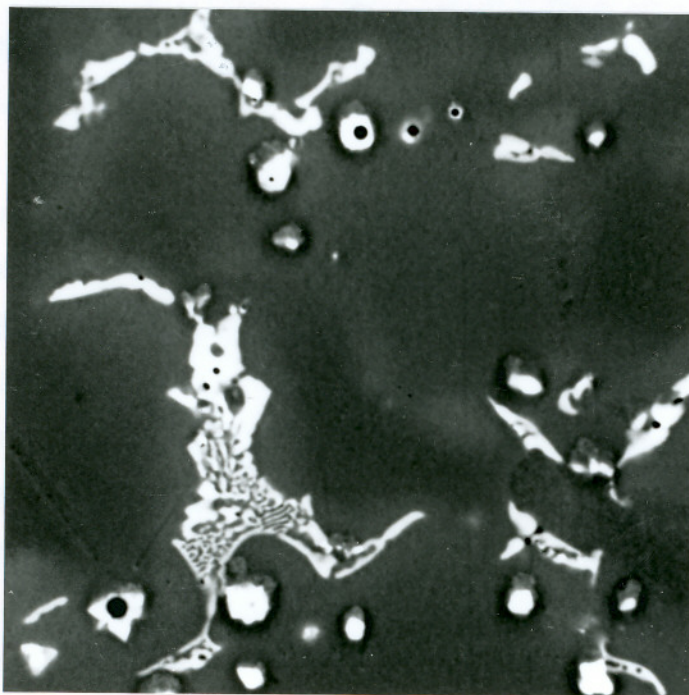


Figure 4. Backscattered Electron Images of the Cladding Microstructure in Conditions (a) ESS, As-Welded, (b) ESS, PWHT, (c) SAS, As-Welded, (d) SAS, PWHT.



5  $\mu\text{m}$

Figure 5. Higher Magnification of Figure 4(d)

#### (d) Transmission Electron Microscopy

Transmission electron microscopy (TEM) was used to identify the interdendritic precipitates formed in the Ni alloy 625 cladding. From selected area diffraction (SAD) pattern analysis, two types of precipitates were found in the cladding deposited by both ESS and SAS, Laves phase and MC carbides. The TEM micrographs taken from the ESS cladding specimens are described in the following text.

Figure 6 shows a TEM micrograph of the interdendritic Laves phase formed in the ESS cladding. Laves phase has a hexagonal crystal structure with lattice parameter  $a = 0.47\text{nm}$  and  $c = 0.77\text{nm}$ .<sup>(34)</sup> Figure 6(a) is a bright field (BF) image and Figure 6(b) is a centered-dark field (CDF) image taken with reflection  $g = [1\ 1\ \bar{2}\ \bar{2}]$ . Figure 6(c) is the SAD pattern taken from the area shown in Figure 6(a), and indexed in Figure 6(d) as a  $[\bar{2}\ 4\ \bar{2}\ 3]$  zone axis.

Figure 7(a) shows the thin-film morphology of the Laves phase solidified at the grain boundaries of cladding deposited by ESS. Figure 7(b) is the SAD pattern related to Figure 7(a). Figure 7(b) is also taken at the  $[\bar{2}\ 4\ \bar{2}\ 3]$  zone axis.

Another morphology of the Laves phase observed was the island shape, as shown in Figure 8(a). Figure 8(b) shows that some small MC carbides are attached to the large Laves phase particle. These carbides are labeled with arrows. This feature can be explained by the carbon rejections. The formula of Laves phase is  $M_2N$ , where  $M$  denotes Ni, Cr or other elements in the matrix and  $N$  denotes Nb or Mo. Laves phase has virtually no solubility for carbon. During Laves phase formation, carbon atoms were rejected from the Laves phase into the matrix/Laves phase boundaries. The accumulation of carbon atoms resulted in the formation of MC carbides.

Figure 9 shows the TEM micrographs of MC carbides formed in the ESS cladding specimens. Figure 9(a) shows the blocky morphology of MC carbides and was taken at  $[0\ 0\ 1]$  zone axis as shown in Figure 9(b). MC carbide has a cubic crystal structure with a lattice parameter of  $a = 0.44\text{ nm}$ .<sup>(34)</sup> Dendritic morphologies of MC carbides were also seen as shown in Figure 10(a). Figure 10(b) is the related SAD pattern in a  $[110]$  zone axis.

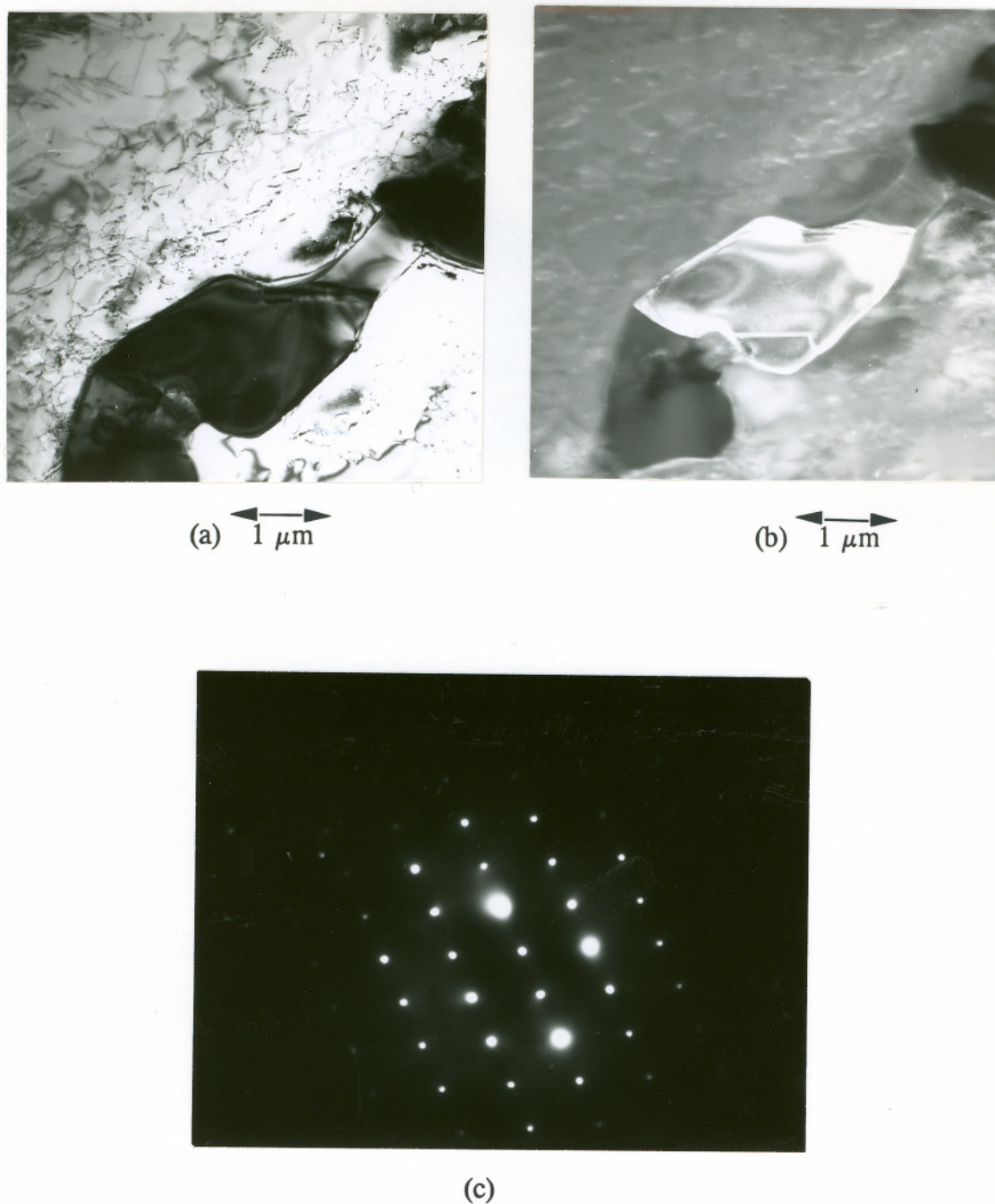
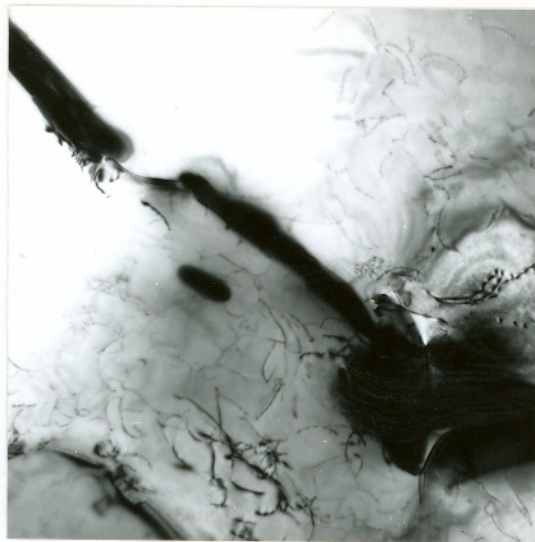
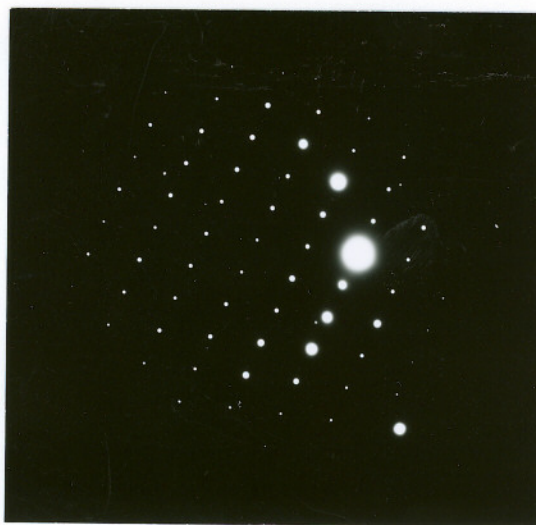


Figure 6. TEM Micrographs of ESS Cladding Showing Laves Phase in (a) Bright Field, (b) Centred Dark Field Taken with Reflection  $[1\ 1\ 2\ \bar{2}]$ , and (c) the Associated SAD Pattern in  $[\bar{2}\ 4\ \bar{2}\ 3]$  Zone Axis.

OSAKA GRADUATE INSTITUTE



(a)  $1 \mu\text{m}$

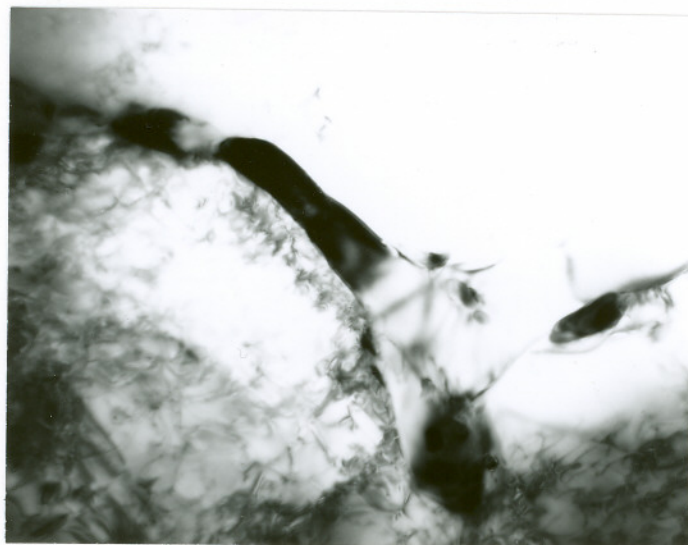


(b)

Figure 7. TEM Micrograph of ESS Cladding Showing Laves Phase in (a) Thin-Film Morphology and (b) the SAD Pattern at  $[\bar{2} 4 \bar{2} 3]$  Zone Axis.

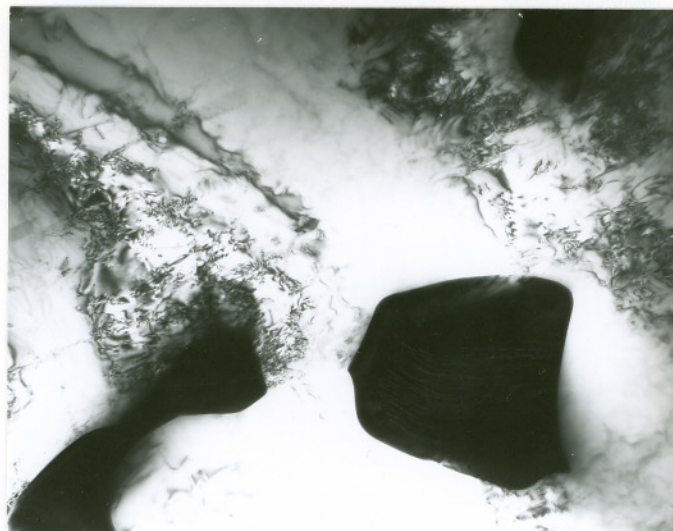


(a)  $1 \mu\text{m}$



(b)  $0.5 \mu\text{m}$

Figure 8. TEM Micrographs of ESS Cladding Showing (a) Laves Phase and (b) Small MC Carbides (Arrows) Attached to the Laves Phase.

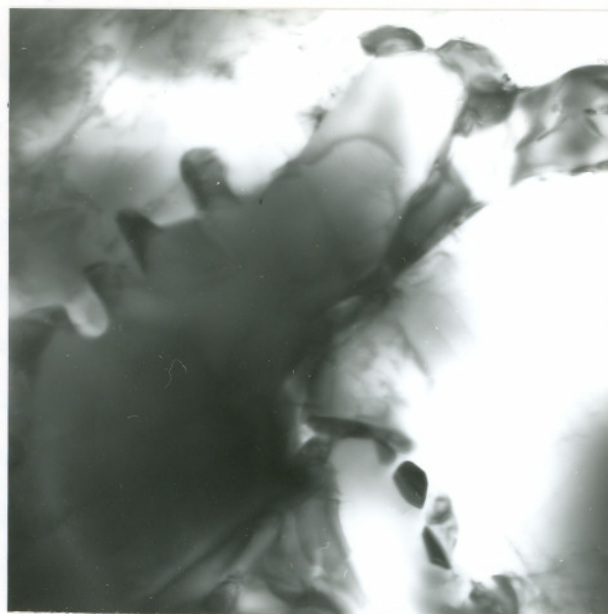


(a)  $\longleftrightarrow$  1  $\mu\text{m}$



(b)

Figure 9. TEM Micrographs of ESS Cladding Showing (a) MC Carbides in Blocky Morphology and (b) the SAD Pattern in [0 0 1] Zone Axis.



(a)  $1 \mu\text{m}$



(b)

Figure 10. TEM Micrographs of ESS Cladding Showing MC Carbides in (a) Dendritic Morphology and (b) the SAD Pattern in [1 1 0] Zone Axis.

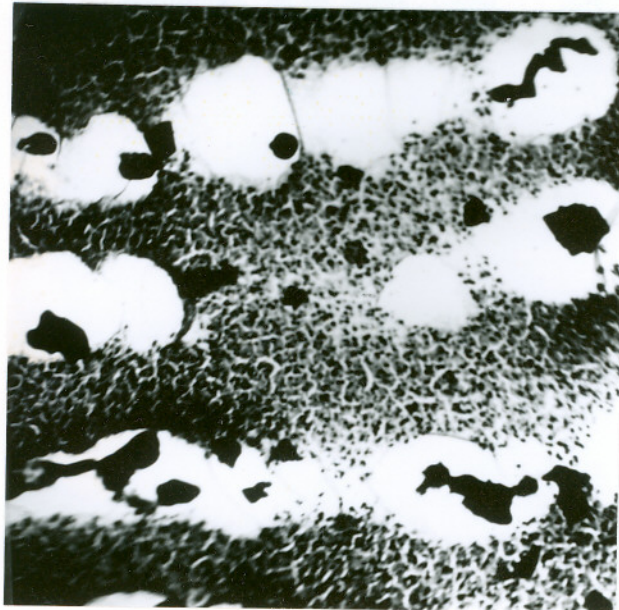
### (e) Extraction Replicas

It was difficult to obtain complete SAD patterns from the interdendritic precipitates in the ESS and SAS cladding due to their large thickness. Therefore, the extraction replica technique was used to determine the phase compositions and provided another way to identify them. With the extraction replica, chemical information from the precipitates can be obtained without any influence from the surrounding matrix.

Figure 11 shows a TEM photo of an extraction replica obtained from the ESS cladding surface. Blocky and dendritic morphologies of MC carbides were observed in the extraction replicas as shown in Figure 12(a) and (b).

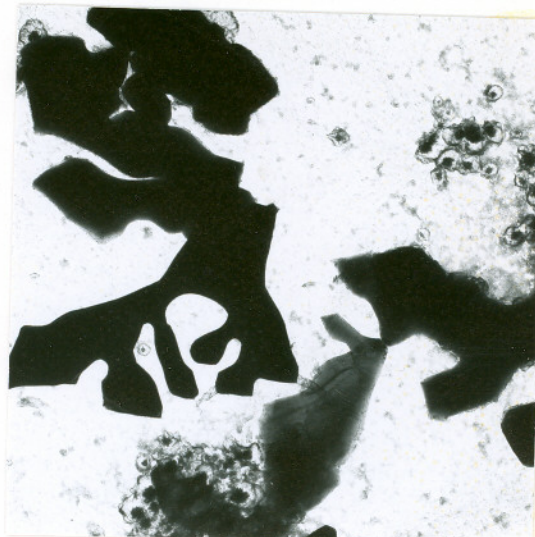
The energy dispersive X-ray spectra of Laves phase and MC carbides are shown in Figure 13(a) and (b), respectively. The Cu peaks were from the copper TEM grids. For Laves phase, Nb and Mo had strong intensity peaks besides the strongest Ni peaks. For MC carbides, the carbon content could not be determined due to the equipment limitation, Nb and Mo were shown to be the two major elements. The chemical compositions, listed in Table 4, of the two primary interdendritic constituents were calculated using a standardless analysis program. The Laves phase contained a high content of Ni, Nb, Mo, Cr, and trace amounts of Fe and Si. The MC carbides consisted of Nb and Mo, and very small amounts of Cr and Ti. Basically, Laves phase and MC carbides are Nb-rich or Mo-rich constituents.

The interdendritic constituents were brighter than the surrounding matrix in backscattered electron images shown in Figure 3. The average atomic numbers of Laves phase, MC carbides and the matrix were estimated. The average compositions of Laves phase and MC carbides are given in Table 4, and the matrix composition in Table 1. The calculated average atomic numbers of the MC carbides, Laves phase and the matrix were about 37, 33 and 26, respectively. This explains why the interdendritic precipitates were brighter in the backscattered electron images.

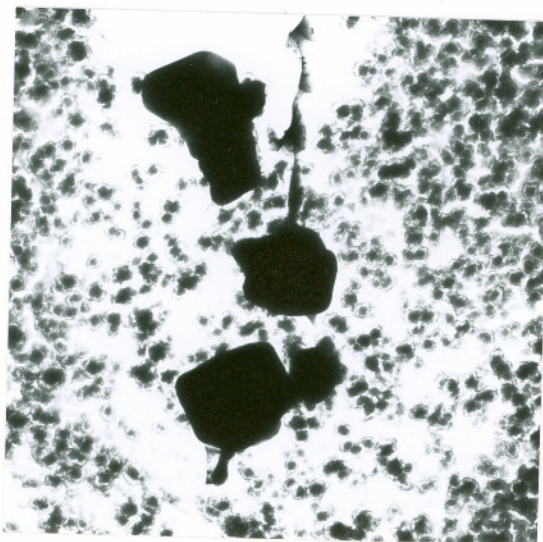


5  $\mu\text{m}$

Figure 11. Extraction Replica Obtained from the ESS Cladding Layer in As-Welded Condition.

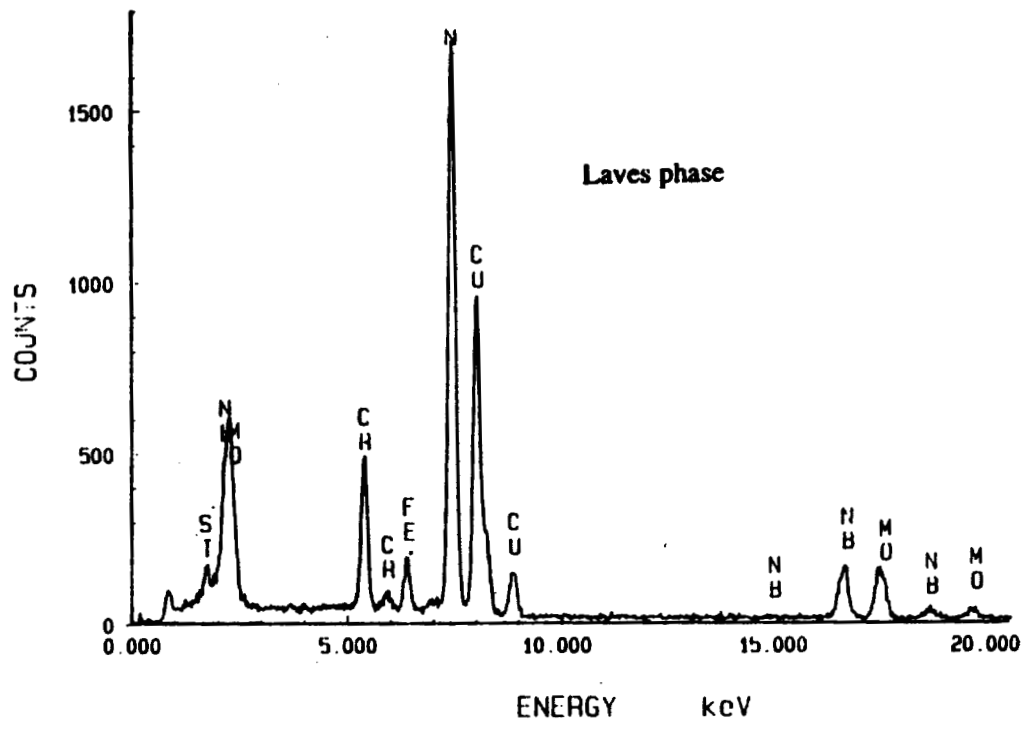


(a) 1.25  $\mu\text{m}$

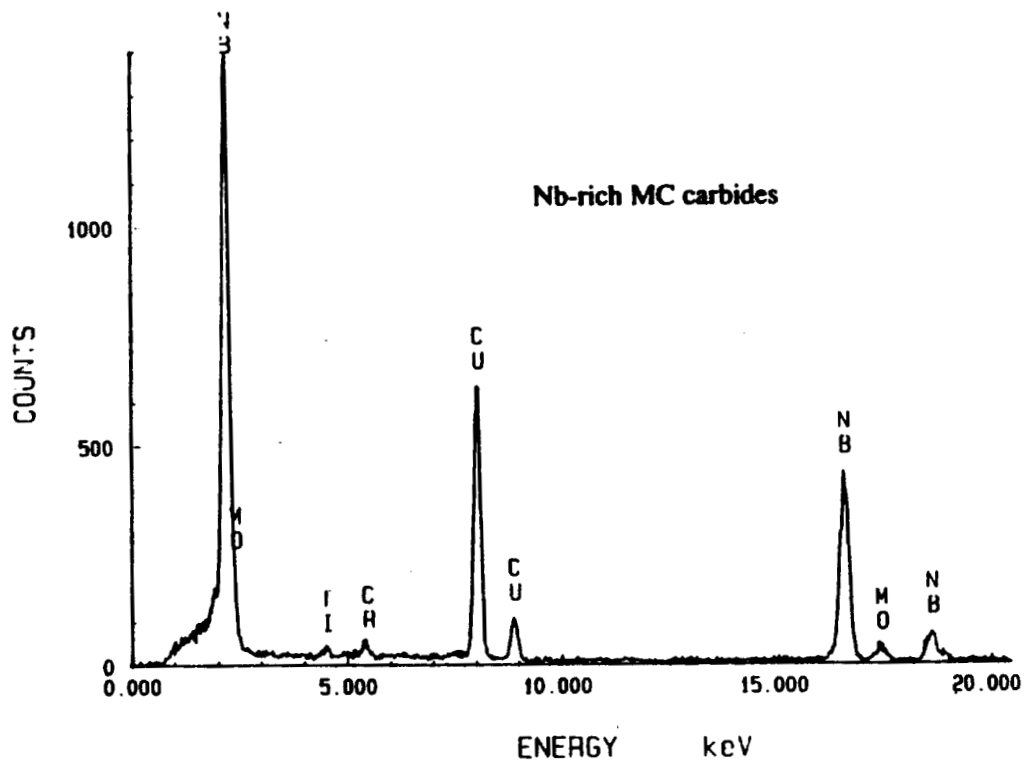


(b) 2.5  $\mu\text{m}$

Figure 12. Extraction Replica of ESS Cladding Showing the MC Carbides in (a) Dendritic and (b) Blocky Morphologies.



(a)



(b)

Figure 13. EDS Spectra of the (a) Laves phase and (b) MC Carbides.

Table 4. Phase Compositions Determined By STEM/EDS							
Phase	Chemical Compositions (wt%)						
	Ni	Nb	Cr	Mo	Fe	Si	Ti
Laves	45.9	11.4	14.5	22.1	5.1	1.0	0
	29.8	25.2	10.6	29.8	3.3	1.3	0
	32.3	14.9	15.9	31.4	3.9	1.6	0
	39.5	12.4	24.6	18.8	3.1	1.6	0
	35.9	16.5	11.5	30.2	3.8	2.1	0
	26.3	14.8	13.2	29.8	4.1	1.9	0
	MC	0	61.8	1.3	36.1	0	0
0		60.7	1.5	37.2	0	0	0.6
0		61.3	0.9	35.5	0	0	2.3
0		58.9	1.9	38.6	0	0	0.5
0		59.3	1.0	38.9	0	0	0.8
0		61.0	1.2	36.6	0	0	1.2
0		60.7	0.7	38.2	0	0	0.4

#### (f) Elemental Segregation

Figure 14 shows the element segregation profiles across the dendrites in the ESS cladding layer in the as-welded condition. The concentration of Ni, Cr and Fe were maximum at the dendrite core (DC) positions, while the concentration of elements Nb, Mo and Si were maximum at the interdendritic core (IC) spaces. The results are consistent with other reports.<sup>(7-8)</sup> Dendritic solidification of the cladding layers caused the observed elemental segregations. Both of the ESS and SAS cladding specimens had similar variation profiles, so only the one from the ESS specimen is shown here.

During solidification of the Ni alloy 625, Nb, Mo and Si were depleted into the interdendritic regions. The higher concentration of Nb, Mo and Si at the interdendritic spaces reduced the solidus temperature of the area, and also promoted the formation of the low melting point eutectic-like  $\gamma$ /MC carbides and  $\gamma$ /Laves phase constituents. The

formation of the low melting point eutectic-like MC carbides and Laves phase promoted by the segregation of Nb, Mo and Si, could cause solidification cracking and degrade mechanical properties. However, no cracks have been observed for either ESS and SAS cladding performed in the current study.

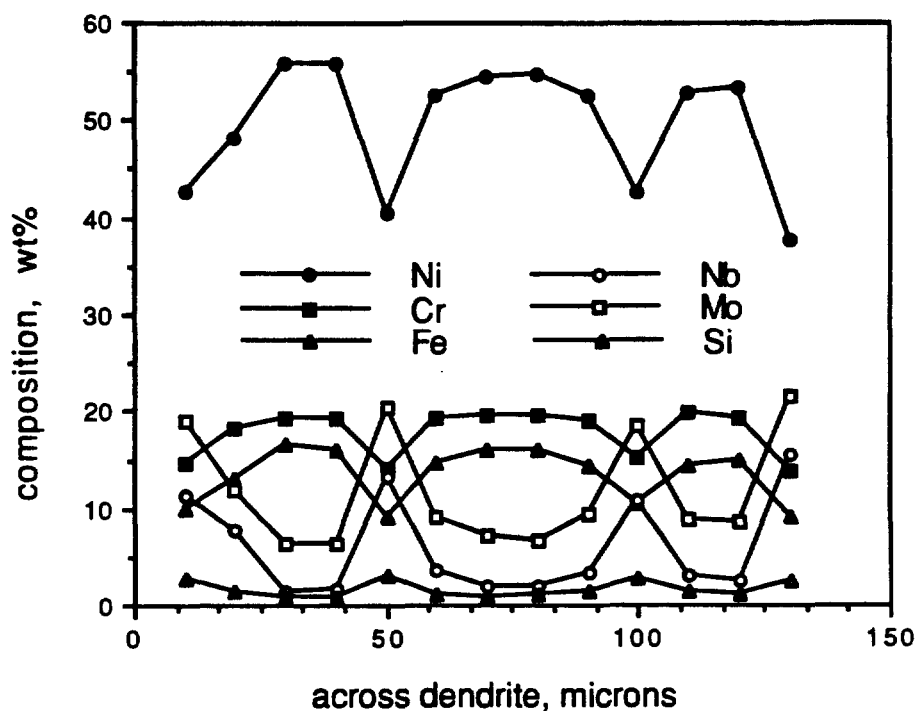


Figure 14. Elemental Segregation Profiles across Dendrites of ESS Cladding in the As-welded Condition.

### 3. Tensile Testing

Tensile specimens were taken from the single layer ESS and SAS cladding (as-welded and PWHT) and were tested at room temperature. The strength and ductility of the cladding layers are shown in Table 5. Compared to the original material of the Ni alloy 625, the yield strength (YS) and the ultimate tensile strength (UTS) were reduced after the ESS and SAS cladding processes. Yield strength of the Ni alloy 625 strip was 71 ksi, and UTS was 124 ksi. The cladding layers had about the same level YS and UTS for the two cladding processes. Yield Strength of the cladding layers was reduced

to about 57 ksi and UTS was reduced to 98 ksi.

<b>Table 5. Tensile Properties of Single Layer Cladding</b>				
<b>Material</b>	<b>YS, ksi</b>	<b>UTS, ksi</b>	<b>% ELONG</b>	<b>% RA</b>
<b>Base Metal</b>	89.5	109.3	21	62.5
<b>Ni Alloy 625 Strip</b>	71	124	50	
<b>As-Welded</b>				
<b>ESS</b>	57	98	50	38.5
<b>SAS</b>	56	97	39	36.5
<b>Post-Weld Heat-Treatment</b>				
<b>ESS</b>	59	101	42	38
<b>SAS</b>	55	98	32	31

Another parameter is ductility, which is a measure of the material's ability to deform plastically. Ductility includes elongation and reduction of area. The cladding layers had lower ductility than the original Ni alloy 625. In comparison with the tensile data of the SAS cladding, the cladding layers deposited by ESS had higher elongation and reduction of area at the same level of YS and UTS. The PWHT reduced the ductility by a small amount.

The ductility of the cladding layers was more sensitive to the cladding process and the heat-treatment conditions than the strength as shown in Table 5. The fracture surfaces of the tensile specimens were examined using SEM and are shown in Figure 15. The fracture surfaces from the ESS cladding layers in the as-welded and PWHT conditions, which had higher ductility than the SAS cladding layers, show an even distribution of the microvoid coalescence in Figure 15(a) and (b). Fracture in the SAS cladding (as-welded and after PWHT) occurred preferentially along interdendritic regions, this is illustrated in the fractographs of Figure 15(c) and (d).

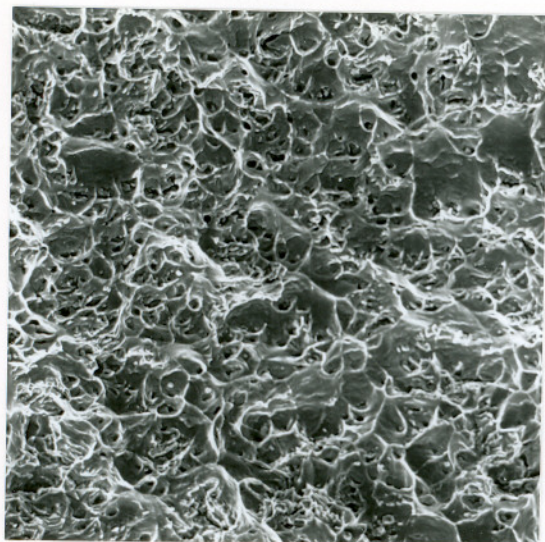
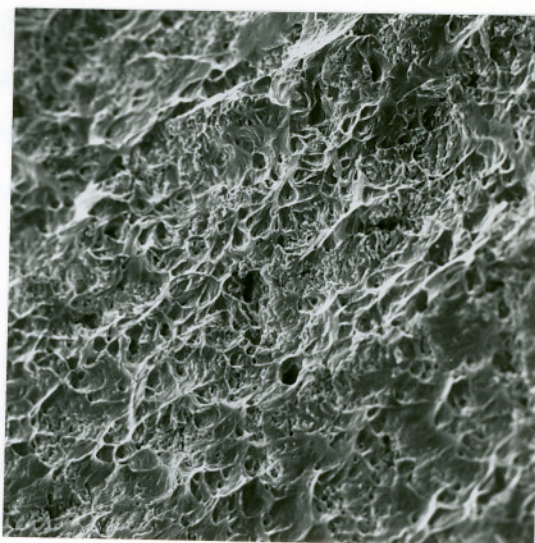
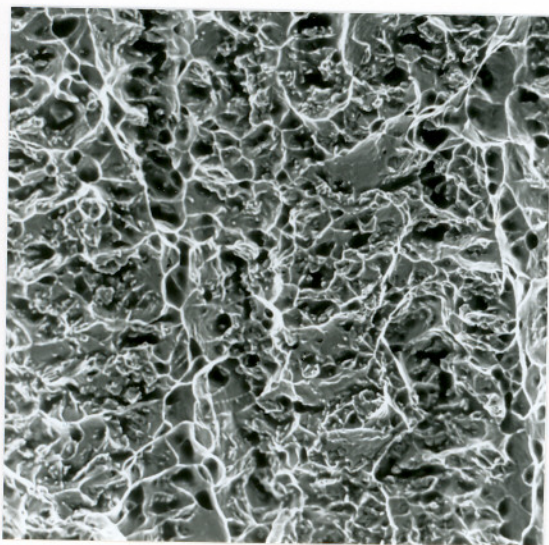
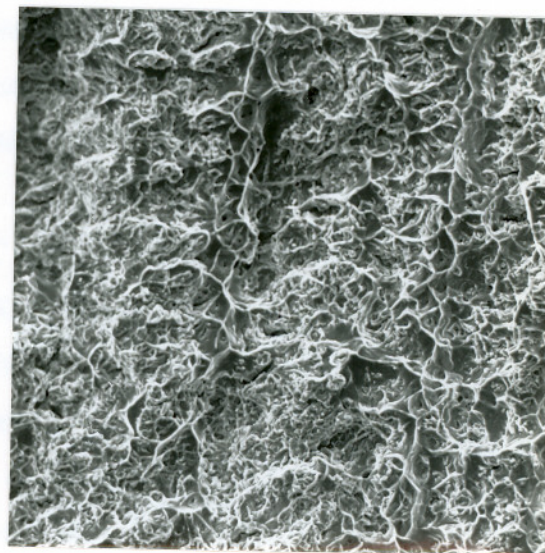
(a) 20  $\mu\text{m}$ (b) 20  $\mu\text{m}$ (c) 20  $\mu\text{m}$ (d) 20  $\mu\text{m}$ 

Figure 15: Fractographs of the Tensile Specimens in Conditions (a) ESS, As-Welded, (b) ESS, PWHT, (c) SAS, As-Welded and (d) SAS, PWHT.

The ductility change can be explained by the difference in the microstructure shown in Figure 2 and 4. Figure 1 shows that there are many large oxide inclusions in the SAS cladding layers. The big brittle oxide inclusions are the crack initiation sites. The microstructure shown in Figure 4(a) and (b) correspond to the fractures shown in Figure 15(a) and (b). The interdendritic MC carbide and Laves phase in Figure 4(a) and (b) were small and isolated from each other, and generally had a blocky morphology. This microstructure resulted in the uniform dimples formed during fracture of the ESS cladding. The precipitates in the SAS cladding layers, Figure 4(c) and (d), were coarse and inter-connected, and most of them had a eutectic-like structure. This coarse and interconnected nature of these eutectic-like structures had a weak bond with the surrounding matrix and provided a low-resistance path to fracture. Therefore, interface fracture between the interdendritic precipitates and the matrix occurred in the SAS cladding (as-welded and PWHT) which is illustrated in Figure 15(b) and (c).

#### 4. Summary

The microstructure of cladding deposited on the low alloy steel with Ni alloy 625 strip electrodes by the ESS and SAS processes, consisted of gamma ( $\gamma$ ) matrix and interdendritic precipitates. Using TEM, the interdendritic precipitates were identified as (Nb, Mo)-rich MC carbides and Laves phase. The Laves phase were observed in block, thin-film and island morphologies. The MC carbides present in blocky and dendritic structures. During the solidification of the ESS and SAS cladding, Nb, Mo and Si were segregated into the interdendritic areas. The high concentration of Nb, Mo and Si in the interdendritic areas reduced the solidus temperatures of these regions and promoted the formation of the (Nb, Mo)-rich MC carbides and Laves phase.

Compared to the SAS cladding, the cladding layers deposited by the ESS had (1) lower Fe, C, Si and O contents, (2) lesser oxide inclusions and, (3) smaller size and lesser area fraction of the interdendritic MC carbides and Laves phase. The higher concentration of Fe and C in the SAS cladding were caused by the higher dilution level during the SAS process. Silicon and O were introduced into the cladding layers as a

result of the metal-slag reactions. The flux used for the SAS cladding contained a large amount of  $\text{SiO}_2$  and other oxides.

Silicon and C played important roles during the solidification of the ESS and SAS cladding. It was reported that additions of C promoted the formation of MC carbides, and silicon increased the formation of Laves phase.<sup>(7-9)</sup> From the analysis of extraction replicas, the Laves phase contained high contents of Nb and Mo and also always had a small amount of Si. The MC carbides were primarily composed of C, Nb and Mo, without containing Si. Therefore, the higher contents of Si and C in the SAS cladding should result in higher amount of interdendritic MC carbides and Laves phase. The carbon content was 0.04% in the ESS cladding layer and 0.05% in the SAS cladding layer, see Table 3. The difference in the C contents of the ESS and SAS cladding layers, regarding the effect on the formation of MC carbides, is considered to be insignificant. However the silicon content difference produced by the two cladding processes can not be neglected. The SAS cladding layer contained 0.69% Si which doubled the amount of the Si content in the ESS cladding. The extra amount of the interdendritic precipitates formed in the SAS cladding compared to the ESS cladding should be attributed to the Laves phase, because Si has no effect on the formation of MC carbides.

Table 6. Solidus Temperature ( $T_s$ ) and the Melting Range ( $\Delta T$ ) of the Cladding		
Temperature ( $^{\circ}\text{C}$ )	ESS	SAS
$T_s$	1285.7	1265.1
$\Delta T$	73.2	83.8

The higher concentrations of Si and C produced by the SAS cladding also affected the solidification behavior of the Ni alloy 625. The solidus temperature and the melting range of the cladding layers by ESS and SAS methods can be estimated using equations [2]-[3], and listed in Table 6. The Ni alloy cladding layers had wider solidification temperature range and lower solidus temperature when using the SAS process. This

promoted the formation of the coarse, inter-connected MC carbides and Laves phase, which has been shown in SEM micrograph Figure 4. The wider melting range in the SAS cladding should also increase the susceptibility to solidification cracking of Ni alloy 625. It has been shown by Gao et al<sup>(1)</sup> that the ESS cladding was more resistant to solidification cracking than similar cladding deposited by SAS.

## B. ESS Cladding Interface Characterization

### 1. Microhardness

Figure 16 shows the knoop hardness number (KHN) variation profiles, from the Ni alloy 625 cladding layers to the low alloy steel for the ESS cladding in the as-welded and PWHT conditions. The microhardness values change sharply from the cladding layer to the HAZ of the base metal steel. The zero position of Figure 16 corresponds to the fusion line. The maximum KHN at the HAZ reached above 400 KHN at the as-welded condition, and then had some drop after PWHT.

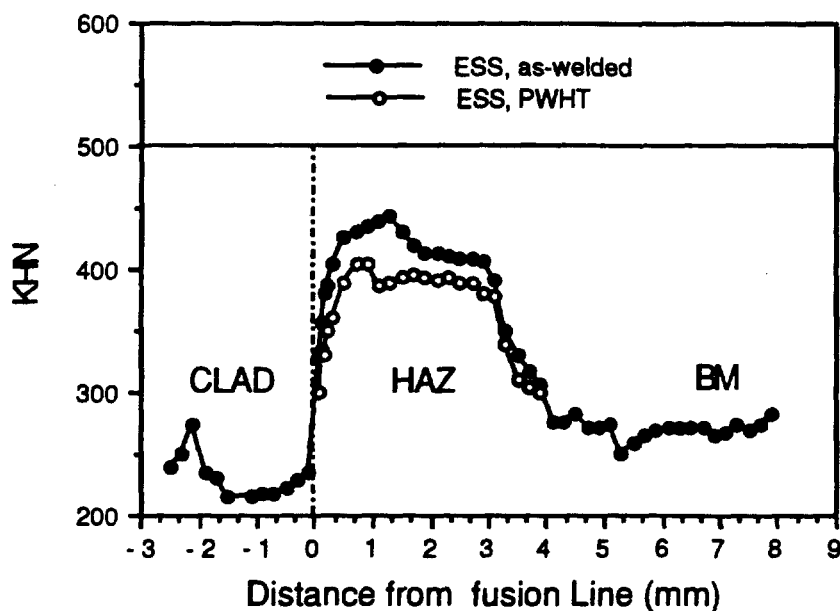


Figure 16. Microhardness Profiles across the Interface of ESS Cladding in the As-Welded Condition.

## 2. Composition Variations

Figure 17 shows the chemical composition profiles across the fusion line. The chemical compositions changed greatly within the 70 micron range from -10 microns (HAZ area) to 60 microns (cladding area). The Fe content dropped from 96% (wt pct) to about 12%, and the Ni increased from less than 5% to 60%. This 70 micron range (from -10 microns to 60 microns) was a transition zone within which mixed compositions of the base metal steel and the Ni alloy 625 strip were contained.

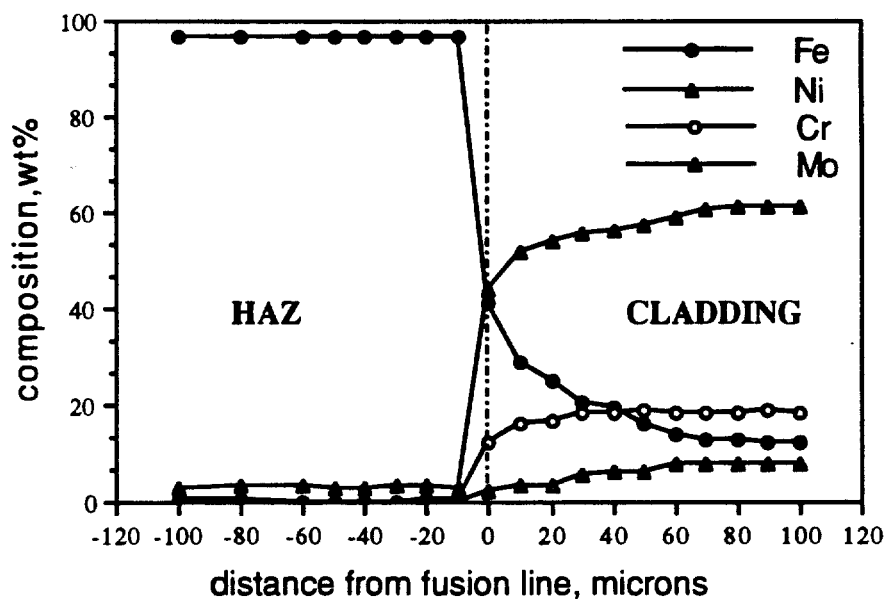
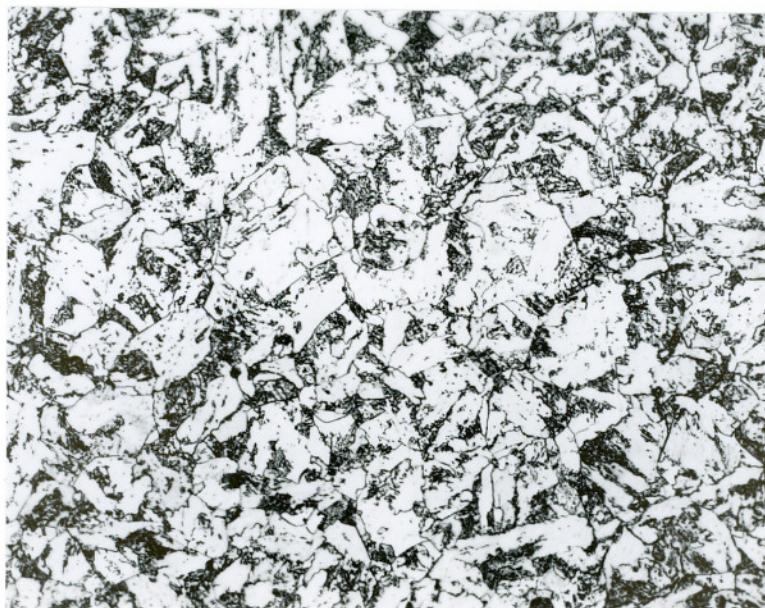


Figure 17. Chemical Composition Profiles across the Interface of ESS Cladding in the As-Welded Condition.

### 3. Optical Microscopy

Figure 18 shows the original microstructure of the base metal steel in the normalized condition, which consisted of ferrite and pearlite. Figure 19(a) and (b) are optical micrographs of the ESS cladding specimens in the as-welded and PWHT conditions, respectively. In Figure 19(a) and (b), the top areas show the microstructure of the Ni alloy 625 cladding layers containing the interdendritic (Nb,Mo)-rich MC carbides and Laves phase; the bottom areas show the coarse grain size region of the HAZ of the steel. There was a subtle difference between Figure 19(a) and Figure 19(b) from the optical micrographs, that is the morphology of the fusion line. The fusion line in the as-welded condition of Figure 19(a) looks very rough with many small Ni-base austenite intrusions (arrows) penetrating into the HAZ. After the heat-treatment, a sharp and smooth fusion line was seen as shown in Figure 19(b). It was difficult to identify the HAZ microstructure using optical microscopy. Therefore, electron microscopy was used to reveal the finer details.



25  $\mu\text{m}$

Figure 18. Optical Micrograph of the Base Metal.



(a)  $50\ \mu\text{m}$



(b)  $50\ \mu\text{m}$

Figure 19: Optical Micrographs of the Cladding Interface Deposited by ESS in Conditions (a) As-Welded, (b) PWHT.

#### 4. Analytical Electron Microscopy

##### (a) ESS Cladding Interface in the As-Welded Condition

Figure 20 shows the TEM micrograph taken from the interface area. Figure 20(a) is a BF image which shows three areas labeled A, B and C. Based on SAD patterns, area A was determined to be fcc austenite ( $\gamma$ ), and areas B and C matched bcc ferrite ( $\alpha$ ). The SAD patterns from these three areas are shown in Figure 20(b), (c) and (d). The middle area B is defined as the interface zone which has a bcc crystal structure and is about 0.5 microns in width. This thin interfacial zone was observed throughout the boundary of the cladding between fcc and bcc structures.

Retained austenite films were seen in some areas of the interface and are shown in the micrograph of Figure 21. Figure 21(a) and (b) are bright field and centred dark field images, respectively. Figure 21(b) was obtained using the reflection  $g = [1 \bar{1} 1]_{\gamma}$ .

The associated SAD pattern is shown in Figure 21(c) and indexed in (d). Figure 21(c) can be indexed as a superimposed pattern of  $[2 1 \bar{1}]_{\gamma}$  and  $[3 1 \bar{1}]_{\alpha}$  zone axes. It is known that the orientation relationship between the fcc austenitic structure ( $\gamma$ ) and the bcc ferritic-structure obeys the Kurdjumov-Sach relationship in low or medium carbon steels, and the Nishiyama-Wassermann relationship in high carbon steels.<sup>(47-52)</sup> From stereographic projections,<sup>(52)</sup> the SAD pattern of Figure 21(c) with  $[2 1 \bar{1}]_{\gamma} // [3 1 \bar{1}]_{\alpha}$  matches with the K-S relationship:  $\{1 1 1\}_{\gamma} // \{1 1 0\}_{\alpha}$ ,  $\langle 0 1 1 \rangle_{\gamma} // \langle 1 1 1 \rangle_{\alpha}$ . Therefore, the retained austenite films and the bcc parent were in K-S orientation relationship.

Figure 22 also shows a TEM micrograph of the interface. Figure 22(a) is a BF image. From the morphology, area T appears to be a twinned structure. However, no extra diffraction spots were seen which was probably due to the weak intensity of the twinning diffraction spots. Figure 22(b) and (c) show the SAD patterns from the left area A (fcc) and right area B (bcc). Based on the chemical composition, the crystal structure and the morphology, the interface zone, about 0.5 microns in width as shown in area B of Figure 20(a), can be considered to be lath martensite.

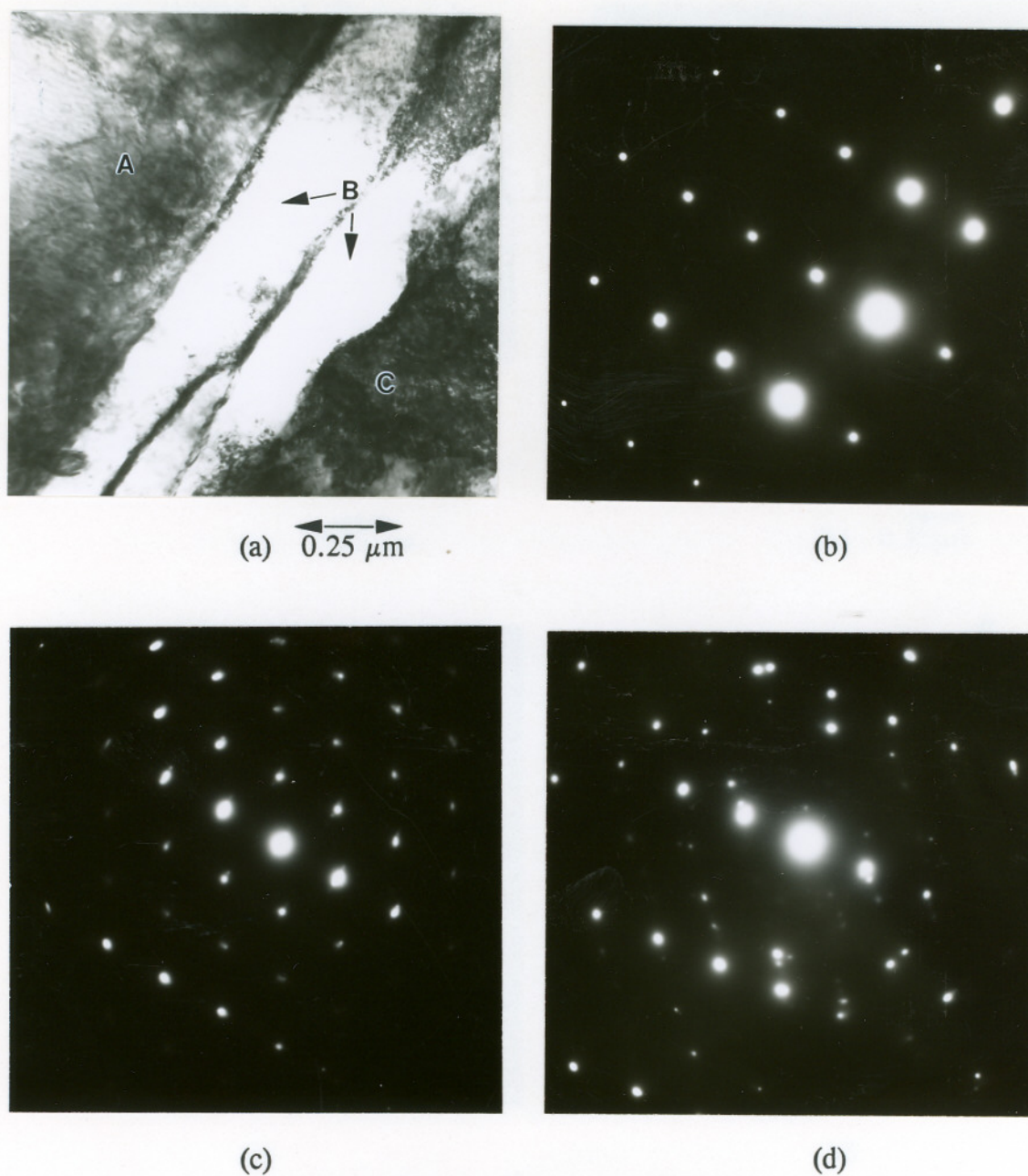
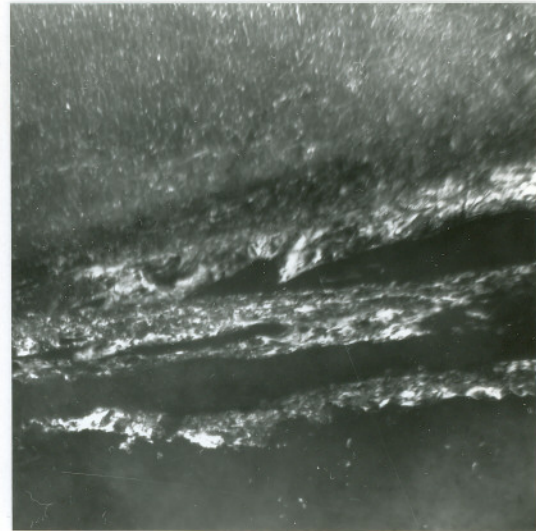
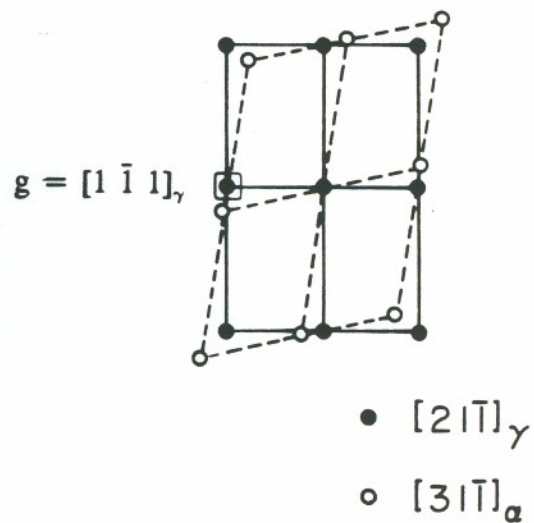


Figure 20. TEM Micrographs of the ESS Cladding Interface in the As-Welded Condition, (a) BF and (b) the SAD Pattern from Area A at  $[0\ 1\ 3]_{\gamma}$  zone axis, (c) SAD Pattern from Area B at  $[1\ 1\ 1]_{\alpha}$  zone axis, (d) SAD pattern from Area C at  $[1\ 3\ 3]_{\alpha}$  zone axis.

(a)  $0.25 \mu\text{m}$ (b)  $0.25 \mu\text{m}$ 

(c)



(d)

Figure 21. TEM Micrographs of the ESS Cladding Interface in the As-Welded Condition Showing the Retained Austenite Films in (a) BF, (b) CDF, Using Reflection  $g = [1 \bar{1} 1]_{\gamma}$  and (c) the SAD Pattern with superimposed zones of  $[2 \bar{1} \bar{1}]_{\gamma}$  and  $[3 \bar{1} \bar{1}]_{\alpha}$  and (d) Index of (c)

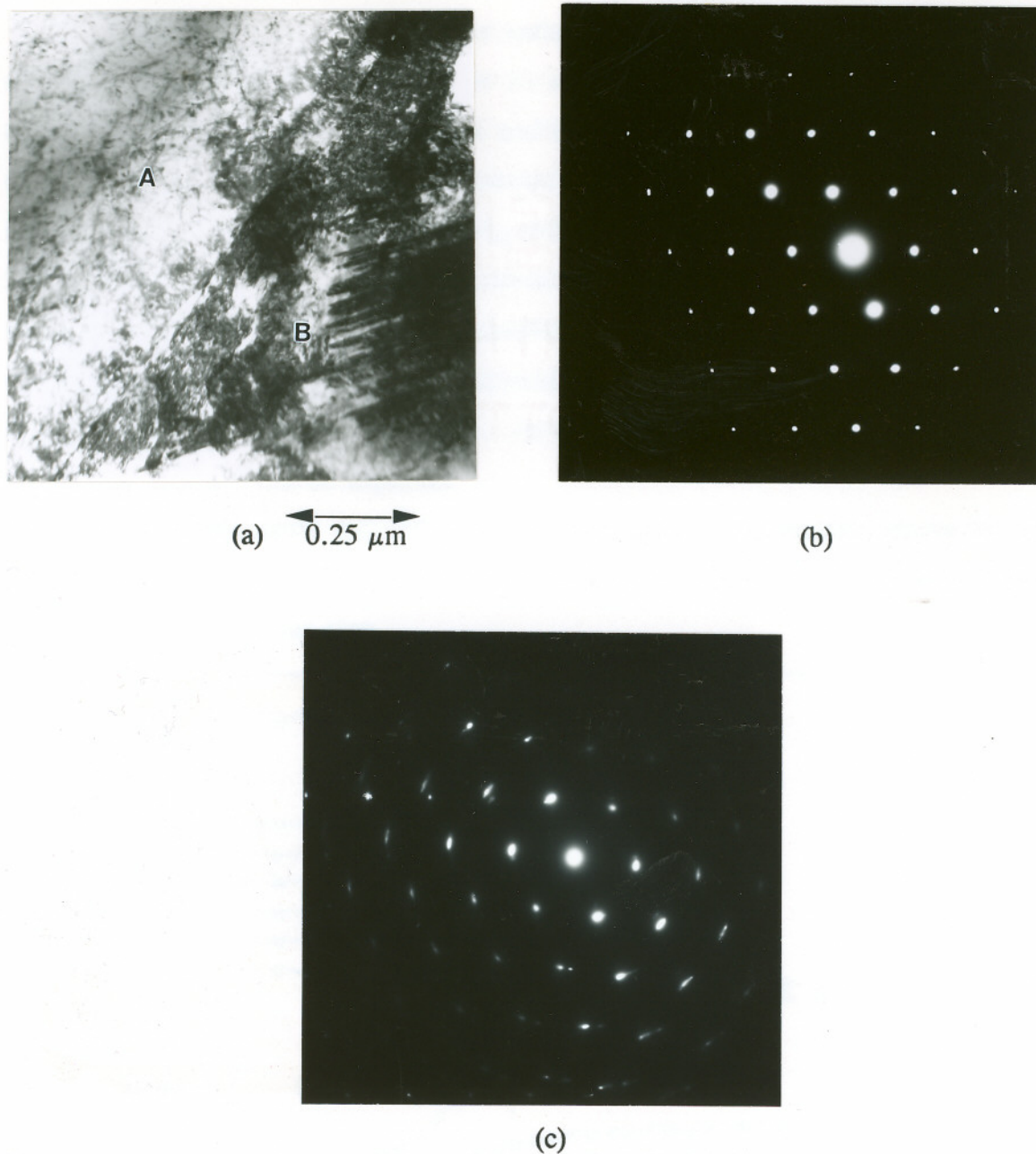


Figure 22. TEM Micrographs of the ESS Cladding Interface in the As-Welded Condition Showing (a) the Fine Twins near the Fusion Line Labelled as T, and (b) the SAD Pattern from area A at  $[0\ 1\ 1]_{\gamma}$  Zone Axis, (c) SAD Pattern from area B at  $[1\ 1\ 1]_{\alpha}$ .

## Chemical Analysis

Figure 23 shows the composition variations across the interface. Zero position corresponds to the boundary between the fcc and the bcc structure. The concentrations of Fe, Ni and Cr were about 60%, 20% and 8%, respectively. From the compositions of Figure 23, it seems reasonable to analyze the microstructure of the interface zone using the Schaeffler diagram.<sup>(53)</sup> The  $Ni_{eq}$  and  $Cr_{eq}$  of each composition point in Figure 23, can be calculated. Different microstructures are predicted from the HAZ to the fcc/bcc interface boundary, using the Schaeffler diagram. At the fcc/bcc boundary, the composition falls into the (austenite + martensite) range. The austenite content decreases as the composition moves to the HAZ. At 0.5 microns away from the boundary, a martensitic structure can be expected.

These results agree well with the TEM observations. Figure 20(a) shows that the interface zone has a bcc structure and is about 0.5 microns in width, within which some retained fcc austenite was seen.

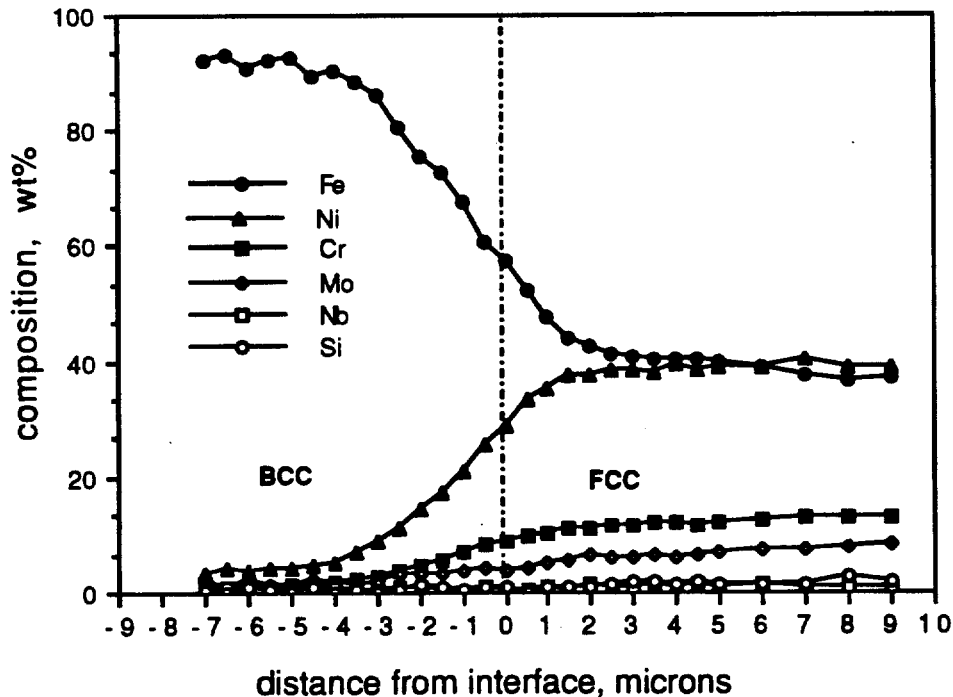


Figure 23. Chemical Composition Profiles across the ESS Cladding Interface in the As-Welded Condition.

### Crystal Structure

The interface zone had a bcc structure, as shown in the SAD pattern of Figure 20. Martensite has a body-centered tetragonal (bct) structure. The tetragonality of the bct structure,  $c/a$  ratio, varies proportionally with the carbon content and follows the equation:  $c/a = 1 + 0.045 \text{ wt}\%C^{(50)}$ . For the materials used in this study, the carbon content in the base metal was 0.25%, and in the filler metal strip was 0.03%. It is possible for the carbon concentration to be higher at the interface region due to the diffusion across the dissimilar metal interface. The mixed morphology of lath and plate martensite with internal twins suggests that the carbon content in this region should be around 0.4%.<sup>(54)</sup> Therefore, a low tetragonality martensite with  $c/a = 1.01$  can be expected. This  $c/a$  ratio is too small to be determined from the SAD patterns.

### Morphologies of the Interface

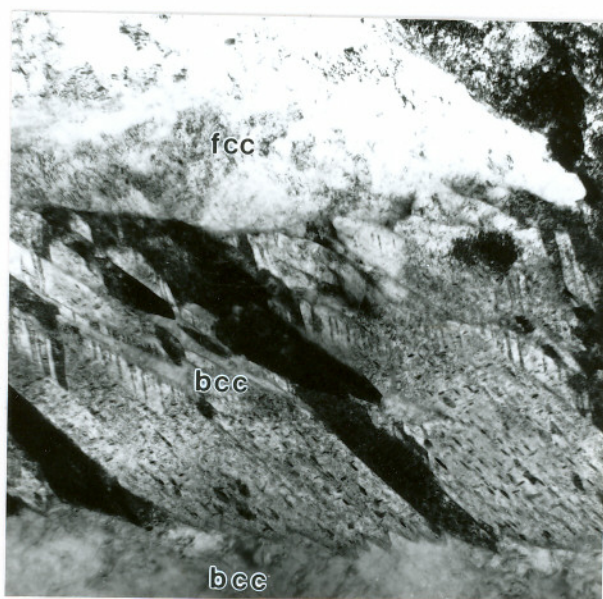
No carbides were present within the interface region. Martensite is a high cooling rate phase transformation product. The atoms, especially interstitial carbon atoms, get trapped inside the lattice of the parent austenite and carbon atom diffusion is inhibited. No carbide precipitation occurred in the untempered martensite.

Figure 22 shows the formation of fine twins. Twinning is the substructure of plate martensite. A high concentration of Ni was measured at the interface area shown in Figure 23. It has been reported that an increase in the substitutional solute concentration, i.e., Ni content, raises the strength and therefore increases the incidence of twinning in alloys, even in the absence of carbon such as in Fe-32%Ni.<sup>(47)</sup>

#### **(b) ESS Cladding Interface after PWHT**

Figure 24 is a TEM micrograph taken from the interface region after PWHT. Fine carbides, in three variants or directions, were present within the martensite region. The interface zone martensite was tempered as a result of the stress-relief heat treatment.

Carbides in tempered martensite and in lower bainite have very similar morphologies, and both of them obey the same orientation relationship relative to the bcc ferrite laths, that is the Bagarazki relationship.<sup>(47)</sup> The difference between the two is that the carbides in the tempered martensite laths usually lie in two or several directions instead of only one direction as in the lower bainite structure.<sup>(49)</sup>



0.5  $\mu\text{m}$

Figure 24. TEM Micrograph of the ESS Cladding Interface after PWHT Showing Tempered Martensite with the Formation of Fine Carbides.

**(c) Summary**

The interface zone was identified to be martensite with about 0.5 microns in width. No carbides were observed in the interface area for the as-welded condition, but some retained austenite films were present. The Kurdjumov-Sach orientation relationship was obeyed between the retained austenite and the low tetragonality martensite. Twinned martensite formed at the interface area as the result of the high concentration of Ni and Cr. After the PWHT, the interface martensite was tempered and fine carbides precipitated inside the laths.

### C. Effect of Preheat Temperature on HAZ Microstructure

Phase transformations within the HAZ of the steel are associated with the thermal cycles. The  $\gamma \rightarrow \alpha$  phase transformation products vary with the cooling rate as shown Figure 25. Preheat temperature has a direct impact on the thermal history of the cladding materials. Prior to the ESS cladding process, the base metal steel plates were preheated to three temperatures: 93°C (200°F), 150°C (300°F) and 204°C (400°F). The preheat process was designed to reduce the cooling rate and avoid the formation of martensite which could cause subsequent HAZ embrittlement. In this study, the HAZ corresponds to the small area next to the interface.

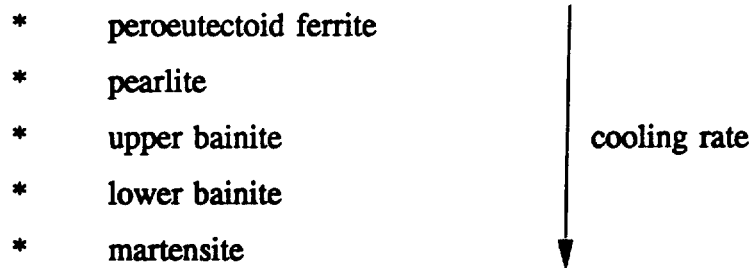
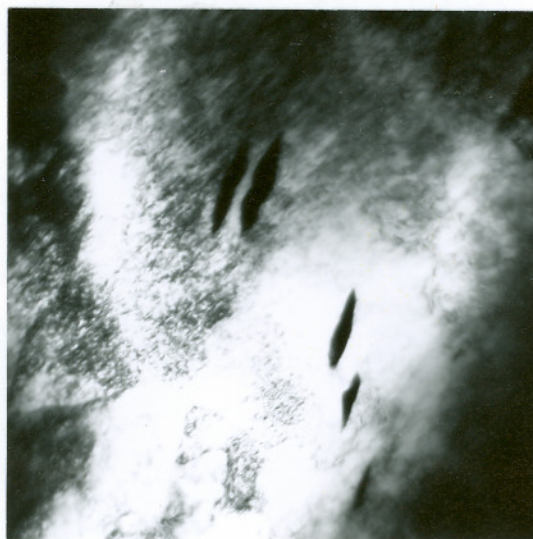


Figure 25.  $\gamma \rightarrow \alpha$  Phase Transformations.

## 1. 93°C Preheat

Figure 26 shows a TEM micrograph of cementite ( $\text{Fe}_3\text{C}$ ) formed within the HAZ. Cementite has a tetragonal crystal structure with lattice parameters of  $a = 0.5089 \text{ nm}$ ,  $b = 0.6743 \text{ nm}$ , and  $c = 0.4532 \text{ nm}$ .<sup>(55)</sup>

The HAZ microstructure of the 93°C preheat specimens primarily consisted of lower bainite and lath martensite. Figures 27 to 28 show the TEM micrographs of the lower bainite constituent. The cementite were formed inside the ferrite laths and had a lenticular morphology. All the carbides were parallel to each other and at about 60° with respect to the main direction of the laths. Lath martensite was another dominant constituent. Figure 29 shows a TEM micrograph of the lath martensite. The laths contained a high density of dislocations.



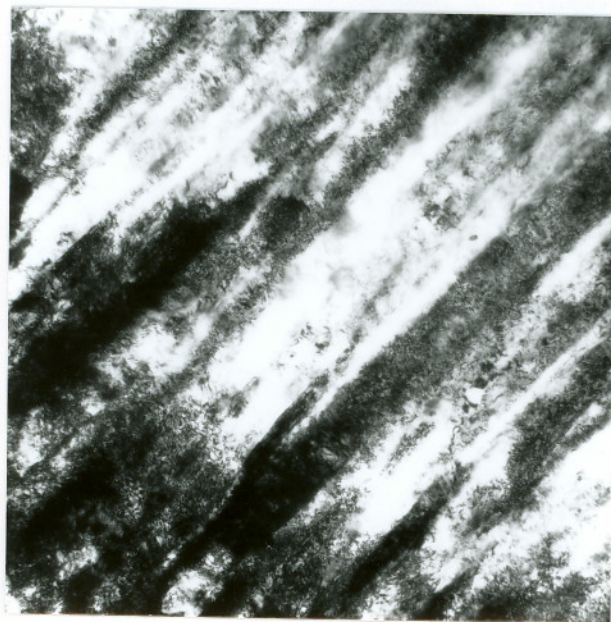
0.5 $\mu\text{m}$

Figure 26. TEM Micrograph of Cementite Formed in the HAZ of the 93°C Preheated Specimens.



1  $\mu\text{m}$

Figure 27. TEM Micrograph of Lower Bainite Formed in the HAZ of the 93°C Preheated Specimens.



0.5  $\mu\text{m}$

Figure 28. TEM Micrograph of the Lath Martensite Formed in the HAZ of the 150°C Preheated Specimens.

## 2. 150°C Preheat

In the 150°C preheated specimens, the HAZ microstructure was dominated by upper bainite and auto-tempered martensite. Compared to the HAZ microstructure in the 150°C preheated specimens shown in Figures 27, the 204°C preheat produced higher amount and larger size of carbide precipitates in the HAZ. Figure 29 is a TEM micrograph of the upper bainite formed in the 204°C preheat condition. It shows that the carbide arrays in the upper bainite lie in one direction.

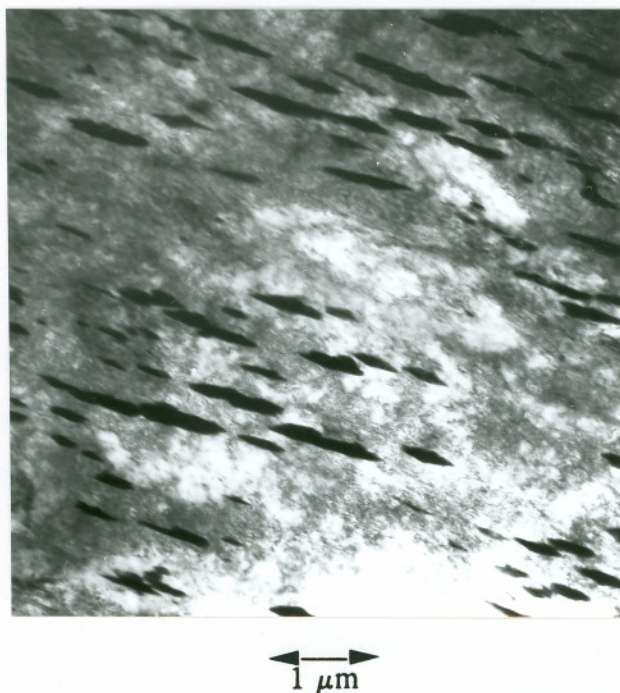


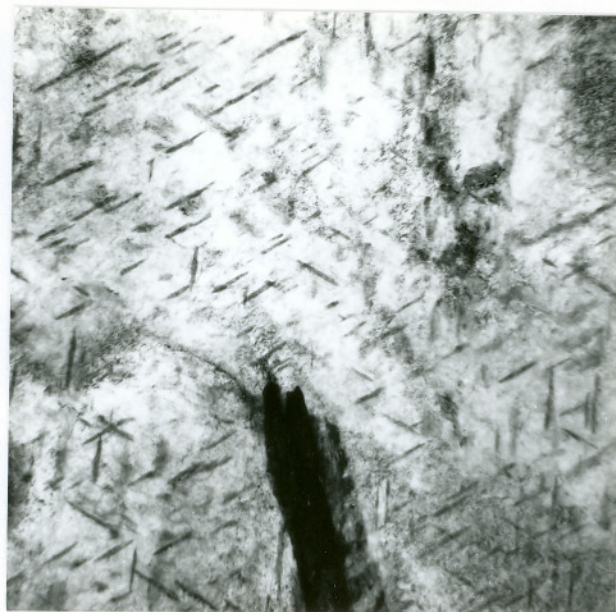
Figure 29. Upper Bainitic Carbides Formed in the HAZ of the 150°C Preheated Specimens.

Figure 30 shows the TEM micrographs of the auto-tempered martensite. Figure 30(a) is a bright field image and Figure 30(b) is a centred dark field image. The carbide morphologies and their number of direction variants formed in the tempered martensite differed from those in the lower and upper bainites. The carbides formed in lower bainite (as shown in Figures 27) or in upper bainite (Figure 29) had a lenticular morphology. While the auto-tempered martensitic carbides had a needle-like shape with very fine size. The carbide precipitates were present in three directions in the auto-tempered martensite instead of only one in the lower or upper bainite. Besides upper bainite and auto-tempered martensite, some other interesting features were also observed such as twinned martensite and carbide precipitates formed on the twins.

Figure 31 shows a TEM micrograph of the twinned martensite. Figure 31(a) is a BF image and Figure 31(b) is a CDF image and thus the twins are seen in opposite contrast. The associated SAD pattern of Figure 31(c) is composed of  $[0\ 1\ 1]_M$  parent zone axis,  $[0\ \bar{1}\ \bar{1}]_T$  twinning zone axis, and double diffraction spots. This matches with the bcc twinning on  $\{1\ 1\ 2\}_\alpha$  planes along  $\langle 1\ 1\ 1 \rangle_\alpha$  directions.<sup>(52)</sup> Figure 31(b) was obtained using the reflection  $g = [0\ \bar{1}\ 1]_T$ , the diffraction spot from the twins.

Figure 32(a) shows the martensite with fine internal twins. By tilting the specimen, some carbides were seen at the sites of the twinned martensite as shown in Figure 32(b). Martensite was formed by a sudden shear due to the high cooling rate, and the plastic deformation field was built-up around the twins. During tempering, carbides precipitated preferentially on the twinning sites where low formation energy was required.

Figure 33 shows another TEM micrograph of the twinned martensite. The morphology was similar to the deformation twins formed in the cold worked microstructure. The black areas were caused by the strain field which was produced as a result of the shear deformation. Some lath martensite was also observed which is shown in Figure 34. Each lath has different level of contrast because of the low angle orientation difference.

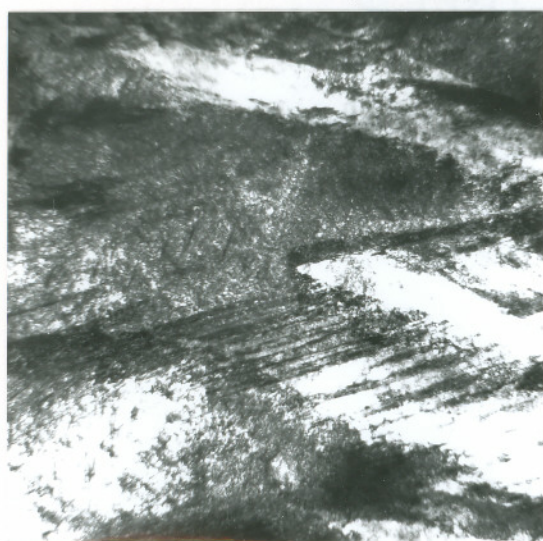


(a)  $\longleftrightarrow$   
0.5  $\mu\text{m}$

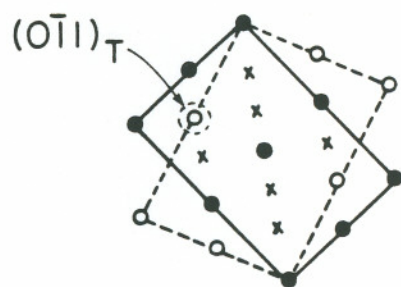


(b)  $\longleftrightarrow$   
0.5  $\mu\text{m}$

Figure 30. TEM Micrographs of the Auto-Tempered Martensite Formed in the 150°C preheated Specimens in (a) BF and (b) CDF Images.

(a)  $0.5 \mu\text{m}$ (b)  $0.5 \mu\text{m}$ 

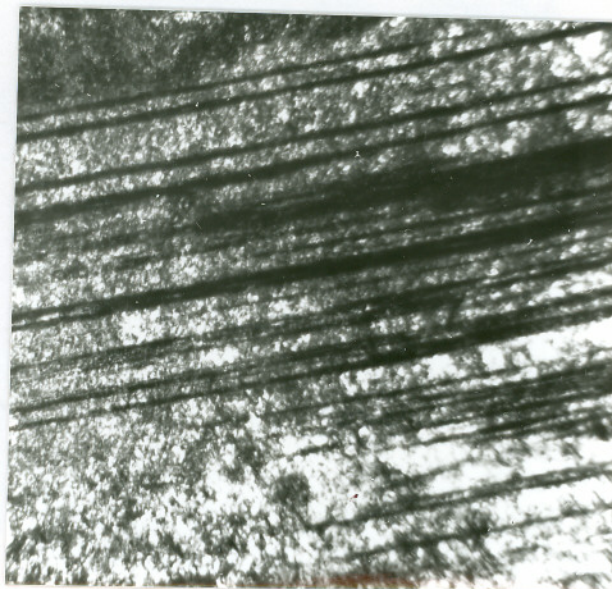
(c)



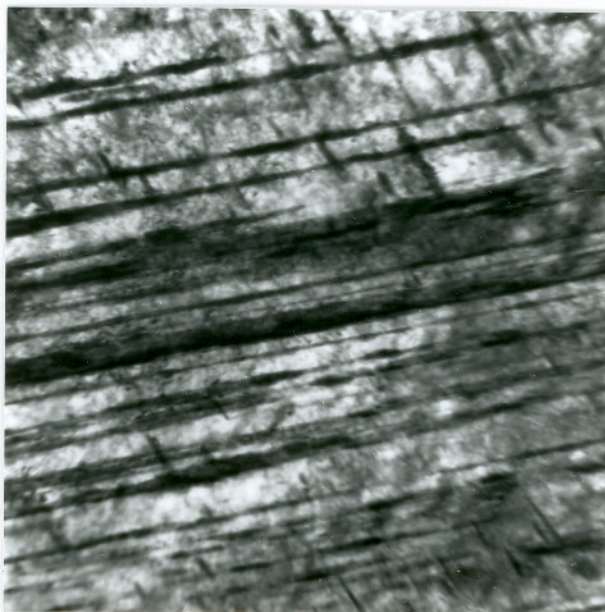
- $[011]_M$
- $[0\bar{1}1]_T$
- x DF

(d)

Figure 31. TEM Micrographs of the Twinned Martensite Formed in the  $150^\circ\text{C}$  Preheated Specimens in (a) BF, (b) CDF, Using Reflection  $g = [0\bar{1}1]_T$ , (c) SAD Pattern and (d) Index of (c).



(a)  $\longleftrightarrow$   
 $0.5 \mu\text{m}$



(b)  $\longleftrightarrow$   
 $0.2 \mu\text{m}$

Figure 32. TEM Micrographs of the Twinned Martensite Formed in the 150°C Preheated Specimens, (a) BF and (b) Carbides Precipitated on the Twins.



↔  
0.5  $\mu\text{m}$

Figure 33. TEM Micrographs of the Twinned Martensite Formed in the 150°C Preheated Specimens.



↔  
1  $\mu\text{m}$

Figure 34. TEM Micrographs of the Lath Martensite Formed in the 150°C Preheated Specimens.

### 3. 204°C Preheat

Auto-tempered martensite was the primary constituent of the HAZ microstructure for the 204°C preheated specimens. Figure 35 shows a TEM micrograph of the auto-tempered martensite. Carbides were formed inside the laths or at the interlath boundaries and two variants or directions of the carbides were seen which were perpendicular to each other.

A small amount of bainite was also seen in this specimen. Figure 36 shows the mixed structure with the lower bainite (labeled as LB) and the upper bainite (labeled UB).

### 4. Summary

The preheat temperature has a strong influence on the HAZ microstructure due to its impact on the cladding thermal cycles. The lower the preheat temperature, the faster the cooling rate. For 93°C preheat, the HAZ went through a shorter time from the peak temperature to room temperature and carbon atoms did not have enough time to diffuse to the grain boundaries or lath boundaries. The cooling rate under this condition favored the formation of lower bainite and lath martensite. As the preheat temperature increased to 150°C, the cooling rate decreased. Some carbon atoms diffused to the boundaries of the parent austenite field as bainitic laths grew. Also the martensite which formed above room temperature was tempered during the dwell time within an elevated temperature range. Therefore, upper bainite and auto-tempered martensite were formed in this condition. For 204°C preheat, the cooling rate was slow enough to allow the carbon atoms diffuse, and accumulate to form the tempered martensite structure.

Hence, as the preheat temperature was progressively increased, the HAZ microstructure changed from [lower bainite + lath martensite], to [upper bainite plus tempered martensite], and to tempered martensite. The HAZ microstructure are summarized in Table 7 for the various heat-treatment conditions.



0.5  $\mu\text{m}$

Figure 35. TEM Micrographs of the Auto-Tempered Martensite Formed in the 204°C Preheated Specimens with Fine Carbides Lying in Three Directions.



0.5  $\mu\text{m}$

Figure 36. TEM Micrographs Showing the Mixed Microstructure of Lower Bainite (LB) and Upper Bainite (UB) in the 204°C Preheated Specimens.

<b>Table 7. Effect of Preheat Temperature on the HAZ Microstructure</b>	
<b>Preheat Temperature</b>	<b>HAZ Microstructure</b>
93°C (200°F)	Lower Bainite + Lath Martensite
150°C (300°F)	Upper Bainite + Tempered Martensite
204°C (400°F)	Tempered Martensite

An interesting feature observed at the HAZ is the twinned martensite. Twinned martensite is the substructure of plate martensite which is usually formed in higher carbon steels. The carbon content was 0.25% in the base metal steel and 0.04% in the Ni alloy strips. So, it is difficult to understand the formation of the twinned martensite in the view of the carbon concentration. However, it should be noted that, the interface and the adjacent HAZ areas contained higher concentration of Ni, Cr and other elements. First, additions of Ni and Cr lower the martensite formation starting temperature  $M_s$ .<sup>(47)</sup> Alloys with low  $M_s$  temperature tend to form plate-like morphologies containing fine internal twins.<sup>(54)</sup> Secondly, high substitutional solute concentrations of Ni and Cr increased the incidence of twinning even in the absence of carbon.<sup>(47)</sup>

## V. CONCLUSIONS

The cladding microstructures of Ni alloy 625 cladding deposited on the low alloy steel using ESS and SAS have been examined. The dissimilar metal joint interface and the HAZ microstructures of the base metal have been characterized using analytical electron microscopy. The primary conclusions and observations resulting from the current work are listed below:

- (1) The cladding microstructure deposited by both ESS and SAS consisted of austenite ( $\gamma$ ) matrix and interdendritic constituents, primarily (Nb,Mo)-rich MC carbides and Laves phase.
- (2) Compared to the cladding deposited by SAS, the ESS cladding had (a) fewer oxide inclusions, (b) less area fraction and smaller size interdendritic MC carbides and Laves phase, and (c) higher ductility.
- (3) The lower tensile ductility of the SAS cladding was related to the formation of coarse, inter-connected, eutectic-like interdendritic (Nb,Mo)-rich MC carbides and Laves phase and the big oxide inclusions.
- (4) For ESS cladding in the as-welded condition, martensite with 0.5 microns in width was present at the interface between the fcc and bcc structures. After PWHT, the interface martensite was tempered resulting in the formation of fine carbides inside the laths.
- (5) The HAZ microstructure of the base metal steel was strongly affected by the preheat temperature for the ESS cladding. As the preheat temperature changed from 93°C to 204°C, the dominant microstructure in the HAZ varied from (martensite + lower bainite), to (upper bainite + auto-tempered martensite), to auto-tempered martensite, respectively.
- (6) Twinned martensite was formed in the steel HAZ due to the high concentrations of Ni and Cr.

## **FUTURE WORK RECOMMENDATIONS**

The present work has studied the microstructure and mechanical properties of the Ni alloy 625 cladding deposited on a low alloy steel by ESS and SAS. Using electron microscopy TEM/STEM, the cladding interface and HAZ microstructure were characterized. The results indicate the necessity of the further study on the following points:

- (1) Corrosion resistance examination of the cladding layers. Elemental segregation formed during the solidification process could affect the pitting and crevice corrosion resistance of the Ni-base alloys.
- (2) Interdendritic low melting eutectic constituents study. Nb-rich MC carbides and Laves phase were observed in the cladding for both ESS and SAS, which would potentially affect the mechanical properties. Therefore, it is very necessary to study the ESS process and control the formation and morphology of the precipitates.
- (3) The effect of the HAZ microstructure upon the mechanical properties. How does the microstructure affect the mechanical properties?

**REFERENCES**

- [1] Y. P. Gao, J. H. Devletian and W. E. Wood, "Electroslag and Submerged Arc Cladding with Nickel Alloy Strip", Proceeding of 3rd International Conference on Trends in Welding Research", ASM International, Gatlinburg, TN, USA, June 1-5, 1992.
- [2] Y. K. Oh, J. H. Devletian, "Electroslag Strip Cladding of Stainless Steel with Metal Powder Additions", Welding Journal, Vol.71(1), January 1992, pp.37-44.
- [3] Y. K. Oh, J. H. Devletian and S. J. Chen, "Low Dilution Electroslag Cladding for Shipbuilding", Welding Journal, Vol.69(8), 1990, pp.37-44.
- [4] Y. K. Oh, J. H. Devletian, "Electroslag Surfacing for Shipbuilding and Repair", Sea Technology, June 1990, pp.46-47.
- [5] A. Van Bemst and Ph. Dargent, "Electroslag Cladding Using Nickel Base Alloys", Metal Construction, December 1983, pp.730-733.
- [6] U. Heubner, T. Hoffmann and G. Rudolph, "Overlay Welding of Corrosion Resistant Nickel Superalloys", in "Weldability of Materials", R. A. Patterson and K. W. Mahin (Eds.), ASM International, Materials Park, OH, 1990, pp.175-182.
- [7] M. J. Cieslak, T. J. Headley, T. Kollie and A. D. Romig, Jr., "A Melting and Solidification Study of Alloy 625", Metall. Trans(A), Vol.19A, Sept. 1988, pp.2319-2331.
- [8] M. J. Cieslak, "The Welding and Solidification Metallurgy of Alloy 625", Welding Journal, Vol.70, February 1991, pp.49s-56s.
- [9] M. J. Cieslak, G. A. Knorovsky, T. J. Headley, A. D. Romig, Jr., "The Solidification Metallurgy of Alloy 718 and Other Nb-Containing Superalloys", Superalloy 718--Metallurgy and Applications, Edited by E. A. Loria, The Minerals, Metals & Materials Society, 1989, pp. 59-68.

- [10] G. A. Knorovsky, M. J. Cieslak, T. J. Headley, A. D. Romig, Jr., and W. F. Hammetter, "Inconel 718: Solidification Diagram", *Metall. Trans.*, Vol.20A, October 1989, pp.2149-2158.
- [11] B. Radhakrishnan, R. G. Thompson, "Solidification of the Nickel Base Superalloy 718: A Phase Diagram Approach", *Metall. Trans.(A)*, Vol.20A, December 1989, pp.2866-2869.
- [12] G. A. Knorovsky and T. J. Headley, "A Microstructural Analysis of Alloy 718 Welds to KOVAR and 304", *Microbeam Analysis*, No.21, 1986, pp.73-77.
- [13] M. C. Maguire, T. J. Headley, "A Weldability Study of HAYNES Alloy 242", in "Weldability of Materials", R. A. Patterson and K. W. Mahin (Eds.), ASM International, Materials Park, OH, 1990, pp.167-173.
- [14] M. J. Cieslak T. J. Headley and A. D. Romig, Jr., "The Welding Metallurgy of HASTELLOY Alloys C-4, C-22 and C-276", *Metall. Trans.(A)*, Vol.17A, November 1986, pp.2035-2047.
- [15] R. G. Thompson, D. E. Mayo and B. Radhakrishnan, "The Relationship between Carbon Content, Microstructure and Intergranular Cracking in Cast Nickel Alloy 718", *Metall. Trans.*, Vol. 22A, February 1991, pp.557-567.
- [16] W.A. Owczarski, D. S. Duvall and C. P. Sullivan, "A Model for Heat-Affected Zone Cracking in Nickel-Base Superalloys", *Welding Journal*, Vol.45, April 1966, pp.145s-155s.
- [17] R. G. Thompson, S. Genculu, "Microstructural Evolution in the HAZ of Inconel 718 and Correlation with the Hot Ductility Test", *Welding Journal*, Vol.62, December 1983, pp.337s-345s.
- [18] R. M. Nugent, "Alloy 625 Surfacing of Tooling and Die Steels", *Welding Journal*, Vol.65, June 1986, pp.33-39s.

- [19] E. G. Thompson, "Hot Cracking Studies of Alloy 718 Weld Heat-Affected Zones", *Welding Journal*, Vol.48, February 1969, pp.70s-79s.
- [20] I. L. W. Wilson, R. G. Gourley and G. J. Bruck, "The Effect of Heat Input on Microstructural and Cracking in Alloy 625 Weld Overlays", in "Superalloy 718, 625 and Various Derivatives", Edited by Edward A. Loria, The Mineral, Metals & Materials Society, 1991, pp.735-746.
- [21] M J. Cieslak, T. J. Headley, and R. B. Frank, "The Welding Metallurgy of Custom Age 625 Plus Alloy", *Welding Journal*, Vol.68, December 1989, pp. 473s-482s.
- [22] W. J. Mills, "Effect of Heat Treatment of the Tensile and Fracture Toughness Behavior of Alloy 718 Weldments", *Welding Journal*, Vol.63, August 1984, pp.237s-245s.
- [23] Government Report Announcement, Vol.85(11), 1985, pp.129-155, "Effect of Iron on the Performance of IN625 Weld Deposites".
- [24] Raghavan Ayer, R. R. Mueller, D. P. Leta and W. J. Sisak, "Phase Transformations at Steel/Clad Interface", *Metall. Trans A*, Vol.20A, April 1989, pp.665-681.
- [25] *Metals Handbook Ninth Edition*, Vol.13, Corrosion, pp.652, ASM International, 1987.
- [26] Sindo Kou, *Welding Metallurgy*, John Wiley & Sons, Inc., 1987.
- [27] Hiroshi Ikawa, Shiegeo Shin and Akihiko Nakano, "Study on Weld Bond of Dissimilar Welded Joint of  $\alpha$  and  $\gamma$ ", *Journal of Welding Institute of Japan (in Japanese)*, Vol. 43(3), 1974, pp.247-257.
- [28] J. T. Tucker, Jr., and F. Eberle, "Development of a Ferritic-Austenitic Weld Joint for Steam Plant Application", *Welding Journal*, Vol.35, November 1956, pp.529s-540s.

- [29] R. W. Emerson, R. W. Jackson and C. A. Dauber, "Transition Joints Between Austenitic and ferritic Steel Piping for High Temperature Steam Service", *Welding Journal*, Vol.41, September 1962, pp.385s-393s.
- [30] F. Gauzzi, S. Missori, "Microstructural Transformations in Austenitic-Ferritic Transition Joints", *Journal of Materials Science*, Vol. 23, 1988, pp.782-789.
- [31] S. J. Matthews and W. F. Savage, "Heat-Affected Zone Infiltration by Dissimilar Liquid Weld Metal", *Welding Journal*, Vol. 50, April 1971, pp. 174s-182s.
- [32] Y. K. Oh, Master Thesis, Oregon Graduate Institute of Science & Technology, 1991.
- [33] G. Seidel and H. Hess, "Investigation of the Electroslag Strip Cladding with Strip Electrodes", *Schweissen Schneiden*, Vol. 23(10), 1971, pp.410-411.
- [34] W. L. Mankins, S. Lamb, "Nickel and Nickel Alloys", *Metals Handbook Tenth Edition*, Vol.2, ASM International, pp.428-445.
- [35] R. A. Muford, "Grain Boundary Segregation in Ni and Binary Ni Alloys Doped with Sulfur", *Metall. Trans.(A)*, Vol.14A, May 1983, pp.865-870.
- [36] George R. Pease, "The Practical Welding Metallurgy of Nickel and High-Nickel Alloys", *Welding Journal*, Vol.36, July 1957, pp.330s-334s.
- [37] M. J. Cieslak and W. F. Savage, "Hot-Cracking Studies of Alloy CN-7M", *Welding Journal*, Vol.64, May 1985, pp.119s-126s.
- [38] W. F. Savage, E. F. Nippes and G. M. Goodwin, "Effect of Minor Elements on Hot-Cracking Tendencies of INCONEL 600", *Welding Journal*, Vol. 56, August 1977, pp.245s-252s.
- [39] Thomas Link, Werner Osterle, "X-ray Microanalysis in the Electron Microscopy, Part IV: Superalloys", *Pract. Metall.*, Vol. 28, 1991, pp.101-114.
- [40] R. Vincent, "Precipitation around Welds in the Nickel-Base Superalloy, INCONEL 718", *Acta Metall.*, Vol. 33(7), 1985, pp.1205-1216.

- [41] F. Schubert, "Temperature and Time Dependent Transformation: Application to Heat Treatment of High Temperature Alloys", Superalloys Source Book, Compiled by Matthew J. Donachie, Jr., pp. 71-111, ASM International, 1984.
- [42] M. J. Cieslak, G. A. Knorovsky, T. J. Headley and A. D. Romig, Jr., "The Use of New PHACOMP in Understanding the Solidification Microstructure of Nickel Base Alloy Weld Metal", Metall.Trans.(A), Vol.17A, December 1986, pp.2107-2116.
- [43] Natsuo Yukawa, Masahiko Moriga, "New Approach to the Design of Superalloy", Japan -- US Seminar in Superalloys, 1985, pp.37-48.
- [44] William A. Owczarski, "Process and Metallurgical Factors in Joining Superalloys and Other High Service Temperature Materials", Superalloys Sourcebook, Compiled by Matthew J. Donachie, Jr., ASM International, pp. 369-400.
- [45] R. A. Patterson and J. O. Milewski, "GTA Weld Cracking -- Alloy 625 to 304L", Welding Journal Vol. 64, August 1985, pp.227s-231s.
- [46] Kenneth Easterling, "Introduction to the Physical Metallurgy of Welding", Butterworths & Co (Publishers) Ltd., 1983, pp.104-154.
- [47] R. W. K. Honeycomb, "Steels -- Microstructure and Properties", ASM, 1981.
- [48] D. N. Shackleton and P. M. Kelly, "Morphology of Bainite", in "Physical Properties of Martensite and Bainite", The Iron & Steel Inst., 1965, pp.126-151.
- [49] G. R. Speich and W. C. Leslie, "Tempering of Steel" in "Phase Transformation and Related Phenomena in Steels", ASM, 1973; or Metall. Trans.(A), Vol.3, May 1972, pp.1043-1054.
- [50] David A. Porter, Kenneth E. Easterling, "Phase Transformations in Metals and Alloys", Van Nostrand Reinhold (UK) Co., Ltd, England, 1987.
- [51] J. H. Devletian, W. E. Wood, "Principles of Joining Metallurgy", in Metals Handbook Ninth Edition, Vol.6, 1987, pp.21-49.

- [52] J. W. Edinton, "Practical Electron Microscopy in Materials Science", Van Nostrand Reinhold Company, 1976, pp.325.
- [53] Handbook of Stainless Steels, Edited by Peckner and Bernstein, McGraw-Hill, Inc., 1977, pp.4-16.
- [54] A. M. Sherman, G. T. Eldis, Morris Cohen, "The Aging and Tempering of Fe-Ni-C Martensite", Metall. Trans.(A), Vol.14A, June 1983, pp.995-1005.
- [55] Metal Physics and Physical Metallurgy, Edited by G. V. Raynor, Vol.4, Pergamon Press, Inc., 1958, pp.923.

### **Bibliographical Note**

The author was born September 21, 1964 in Henan Province, China. She received her BS and MB degrees in Materials Science & Engineering from Central-South University of Technology, Changsha, China in 1985 and 1988, respectively.

She had worked for two years in China National Non-Ferrous Metals Industry Corp.(CNNC) in Beijing, China. Since September of 1990, she joined the Oregon Graduate Institute of Science & Technology, Beaverton, Oregon, and finished the requirements for the degree of Master of Science in Materials Science & Engineering in October, 1992.